Design Tool for Extrusion Based Additive Manufacturing of Functionally Enhanced Lightweight Concrete Wall Elements with Internal Cellular Structures

Wissenschaftliche Arbeit zur Erlangung des Grades
Master of Science
an der Ingenieurfakultät Bau, Geo Umwelt der
Technischen Universität München.

Betreut von   Dr.-Ing. Dipl.-Wirtsch.-Ing. Klaudius Henke

Lehrstuhl für Holzbau und Baukonstruktion

Prof. Dr. sc. ETH Kathrin Dörfler

TT Professorship Digital Fabrication

Fakultät für Architektur

Eingereicht von   Fabian Jaugstetter

Studiengang Energieeffizientes und nachhaltiges Planen und Bauen

Eingereicht am   München, den 01.04.2020

Kurzzusammenfassung

Im Vergleich zur Herstellung einfacher Geometrien, können mit der Technologie der additiven Fertigung auch komplexere Geometrien ohne großen Produktionsmehraufwand hergestellt werden. Diese geometrische Freiheit kann dazu verwendet werden, zusätzliche Funktionen im Druckprozess zu integrieren. Für die Anwendung im Bauwesen existieren bereits Verfahren für das dreidimensionale Drucken mit Beton. Additiv gefertigte Leichtbetonelemente könnten dabei durch interne Zellstrukturen und gleichzeitige geometrische Freiheit so funktionalisiert werden, dass der Materialeinsatz gegenüber konventionellen Konstruktionen reduziert werden könnte. Bei der Planung der Geometrien müssen allerdings materialtechnische Eigenschaften des Betons berücksichtigt werden. Ziel dieser Arbeit ist es daher, ein Designwerkzeug zu entwickeln, welches die Gestaltung von Wandelementen mit internen Zellstrukturen ermöglicht. Deren Druckbarkeit sowie thermische Isolationsleistung soll dabei unter Berücksichtigung der Prozessparameter während dem Designprozess abgeschätzt werden können.

Ausgehend von einer Analyse raumfüllender Körper wurde die Form eines Oktaederstumpfes gewählt, um geschlossene Zellstrukturen geometrisch abzubilden. Die Druckpfade wurden durch eine Sequenz von Vektoren parametrisch so modelliert, dass der Druck kontinuierlich, also ohne Unterbrechungen erfolgen kann. Berechnungen von Überhängen und Schichtumlaufzeiten wurden zur Abschätzung der Druckbarkeit herangezogen. Die Wärmedämmeigenschaften der Strukturen wurden über die Berechnung von Wärmeübergangskoeffizienten abgeschätzt. Die Machbarkeit der Entwicklung wurde abschließend durch die experimentelle Fertigung zweier Demonstratoren evaluiert. Das physische Druckexperiment konnte die prinzipielle Machbarkeit von 3D-gedruckten Zellstrukturen innerhalb von frei geformten Wandelementen aus Leichtbeton bestätigen. Obwohl sich die Überhänge während dem Druckprozess als grundsätzlich stabil erwiesen, kollabierten einige Zellen mit sehr großen Überhängen, wenn sie nicht von benachbarten Zellen unterstützt waren. Im Vergleich zu einem massiven Wandelement konnte gezeigt werden, dass ein Wandelement mit inneren Zellstrukturen die gleiche wärmedämmende Funktion mit weniger Materialeinsatz erreichen kann. Das ideale Verhältnis von Zellvolumen zu Beton ist dabei allerdings abhängig von der verwendeten Druckauflösung.

Abstract

With the technology of additive manufacturing, complex geometries can be produced without additional effort in comparison to the production of simple geometries. This geometrical freedom can be used to integrate additional functions in the printing process. For the application in building construction, processes already exist for additive manufacturing with concrete. Additively manufactured lightweight concrete building elements could be equipped with additional functionality by printing them with internal cellular structures and with a high degree of geometrical freedom. The material input could thus be reduced in comparison to conventional constructions. Even so, process constraints have necessarily to be considered in the design of the geometries. For that purpose, this thesis aims at developing a simple tool for designing wall elements with internal cellular structures with the ability to evaluate the performance and printability of cellular structures under consideration of the lightweight concrete printing related process constraints.

Based on an analysis of space filling volumes, the shape of a truncated octahedron was used to geometrically remodel closed cell structures. A fully parametric approach based on a sequence of vectors was applied to model print paths with continuity implemented inherent in the design system. Calculations of overhangs and layer cycle times have been implemented to predict the printability of the geometries during the design process. Calculations of heat transfer coefficients were applied to estimate the thermal performance also during the design process. The feasibility of the development was then evaluated by experimentally manufacturing two demonstrator objects with lightweight concrete.

The physical printing experiment succeeded in demonstrating the feasibility of manufacturing freeform wall elements with internal cellular structures based on a continuous print path. While overhangs proved to be fundamentally stable, cells with extremely large overhangs collapsed during the printing when they were not supported by neighboring cells. Based on the performance estimation, the additively manufactured element is expected to achieve the same performance as a massive element but with less material. Limitations could be identified regarding the effect of low print resolution on the ideal cell volume to concrete ratio.

Table of contents

List of abbreviations

2D – Two Dimensional

3D – Three Dimensional

AM – Additive Manufacturing

CAD – Computer Aided Design

EIFS – Exterior Insulation and Finish System

FDM – Fused Deposition Modelling: Common process of extrusion-based 3D printing

FEM – Finite Element Method

Glossary

Additive manufacturing: Process of producing three dimensional objects by depositing a material layer by layer. Can also be referred to as 3D printing, layered manufacturing, solid freeform fabrication and others (Gardiner, 2011, p.41)

Cement Hydration: Chemical reaction of cement and water leading to a hardening of concrete

False color rendering: Image based representation of simulation results based on a mapping of results to color ranges

Finite Element Method: Numerical method applied for solving physical problems based on small entities of a larger complex system.

G-Code: Programming language used to describe machine commands in automated fabrication. The name G-Code originates from the fact that many commands used to start with the letter 'G'.

In-situ fabrication: Fabrication of structures directly at their final destination

Mono material construction: Construction composited of only a single material or materials of the same material group. Usually applied to ease recycling and reuse.

Parametric modelling: Method of modifying digital models based on numerical and algorithmic parameters instead of manual inputs

Point: Position in space defined by x, y, z coordinates in Euclidean three space.

Print path: Ordered list of points in space which a robot should follow. The path is a pure geometric description of the planned robot movement.

Trajectory: Robot motion path including velocities and accelerations (Hlaváč, 2019)

1. Introduction

1.1. Motivation

Climate change has become the most crucial of the world's environmental problems. Carbon dioxide is regarded as the main driving force of climate change. With 38% of global greenhouse gas emissions and 40% of global energy use, the building sector is a major burden for the environment (IPCC, 2014).

Resource scarcity and waste are crucial as well: About 50% of all raw materials are being used in the building industry. Globally, 62 gigatons of materials are being processed annually. In contrast, only four gigatons of waste are being recycled so far. More than 40% of the world-wide waste production originate from the building sector. (UNEP, 2012)

Production of cement alone accounts for about 8% of worldwide CO_2 emissions (Lehne and Preston, 2018, p.6). Nevertheless, it is an immensely popular construction material. It is not only cheap, but also very durable, powerful and versatile (Bos et al., 2016, p.209). Architects have always appreciated the creative freedom they could explore when building with concrete. Unfortunately, building with concrete comes with several drawbacks:

As fresh concrete is a near liquid material, it can simply be poured in any desired formwork. Especially freeform, non-standard geometries however, require also complex formwork which involves a high degree of human powered effort and produces costs and waste. In concrete construction, formwork typically accounts for about 40% of the total construction cost (Kothman and Faber, 2016).

A high degree of hard manual work also makes construction sites a dangerous place to work. Compared to other industries, the construction sector still has among the highest rates of work related fatal and non-fatal accidents (eurostat statistics, 2014). Digital fabrication could help at alleviating this issue by doing dangerous tasks robotically.

Conventional concrete, at a density of 2000 kg/m^3, has a thermal conductivity of about 1,6 W/m*K and is therefore not suitable as an insulation material (DIN 4108-4, 2017).

To meet the requirements of highly insulated buildings, concrete walls have thus to be equipped with added layers. Especially when applied as Exterior Insulation and Finish Systems (EIFS) these additional layers are hard to recycle (Albrecht and Schwitalla, 2015, p.7).

With growing awareness for efficiency and sustainability, innovative technologies with the aim of overcoming inefficiency and environmental problems are being developed. Digital fabrication is such a development that can have an impact on the efficiency and environmental sustainability of constructions. Digital fabrication is the combined design and manufacturing process that involves digitally designed computer models to directly control the machinery in the manufacturing process. The manufacturing process in digital fabrication is usually either of subtractive or additive nature. Subtractive processes form a solid peace of material by removing material through processes like cutting or milling. Additive manufacturing, as it is the subject in this thesis, is the process of producing three dimensional objects by adding material layer by layer (Crump, 1992).

In contrast to other industries, where mass production is widespread practice, buildings are usually unique and adapted to a specific local site and context. Additive manufacturing comes in handy at this point because it allows a highly customized production of freeform building elements at no extra effort. Furthermore, additive manufacturing offers to integrate additional functions during the printing process and thus reduce the amount of materials consumed.

1.2. Problem statement

Additive manufacturing is nowadays standard practice in many industries and has revolutionized the way digitally designed objects can become reality. Small three dimensional (3D) printers are even available as affordable consumer products for use at home. Even though the news of 3D printed houses in China (WinSun3D, 2013) made headlines already years ago, additive manufacturing in the construction industry is still in an early phase of development (Bos et al., 2016, p.210). Among challenges in material and process development, a lack of design tools specified for the process and material constraints in additive manufacturing with concrete hamper the development of the technology (Buswell et al., 2018, p.37).

The environmental impact of the 3D printing process itself is relatively low in comparison to materials production (Agustí-Juan and Habert, 2017, pp.18–19). The extra effort of the machinery in the printing process is hence neglectable. Nevertheless, additive manufacturing technologies can only unfold their full potential when they are applied to customized complex geometries with added functionality instead of standard geometries that could be produced conventionally as well.

Increasing material efficiency and integrating additional functions in the manufacturing process reduces material usage and waste production (Agustí-Juan and Habert, 2017, pp.18–19). The potential to reduce material consumption through added functionality and strategic material placement in 3D printing is thus high.

By replacing rocks and sand with lightweight porous aggregates such as expanded glass or wood chips, the insulating properties of concrete can be improved (Henke, Talke and Winter, 2016, p.4). Lightweight concrete is thus already a material that is itself multifunctional. By adding internal voids inside the building element (Buswell et al., 2007, p.230) the insulating properties could be further improved. Therefore, 3D printing provides the opportunity to combine load bearing, room enclosing, aesthetic and insulating functions in a single building element. Building components such as wall elements could thus be produced as single material constructions with multiple functions. By avoiding additional layers such as the common EIFS, recyclability of such elements could be improved. Formwork could become obsolete and even complex geometries could be realized without additional effort.

This thesis aims at exploring multifunctionality in building elements produced by extrusion based additive manufacturing with lightweight concrete. In particular, the feasibility of printing internal cellular structures for the function of enhanced thermal insulation properties shall be studied. The research goal of this thesis can be summarized with these four main objectives:

- Explore the feasibility of extrusion based additive manufacturing of cellular structures inside lightweight concrete building elements.

- Develop a process constraint aware design tool for the print path planning of cellular concrete structures, their graduation and embedding in a freeform wall element.

- Estimate the performance of the geometries regarding printability and thermal insulation.

- Verify the feasibility of the development by manufacturing a demonstrator element.

The research question is thus formulated as follows:

- How can lightweight concrete wall elements be additively manufactured with internal cellular structures and how can their performance regarding printability and thermal insulation be estimated during the design process?

1.3. Method

Literature review is used to contextualize this work in relation to state-of-the-art research and outline the fundamentals of building scale additive manufacturing. The review is based on research papers and doctoral theses in this field. Research of cell structures in other fields and infill patterns in small scale 3D printing are taken as reference as well.

A reconstruction approach is used to get an idea of print paths for internal void structures. This is realized by first 3D modelling closed cell structures and then cutting these in horizontal slices. From the analysis of this "top-down" approach, the actual print paths are parametrically remodeled from scratch.

The development is based on the quite common 3D modelling software *Rhinoceros 6.0* (McNeel & Associates, 2019) in conjunction with the parametric modelling environment *Grasshopper* and the programming language *Python 2.7* (Python Software Foundation). Rhino and Grasshopper are used due to their wide recognition in the field of architecture and construction and their easy extendibility. The Python code is written based on the Rhino Python framework inside Iron-Python. The computational development of this thesis is provided as Python library and Grasshopper plugin with a code documentation provided in Appendix B. Making the tool accessible to other researchers is supposed to ease further optimization of the structure or application in other use cases.

A physical case study experiment eventually assesses the feasibility of the developed design tool. A 6-axis KUKA (KUKA) industrial robot is used to print the developed geometry with a lightweight concrete mixture.

1.4. Structure of the thesis

This thesis is structured in six chapters as described below:

Followed by this introductory section, the second chapter outlines the fundamentals of building scale additive manufacturing by reviewing historic and current research in this field. Literature review is used to collect a state-of-the-art overview of extrusion-based additive manufacturing and functionalities incorporated in the printing process. From this broader context, the focus is drawn towards internal voids in concrete structures and the respective print path modelling.

The third chapter describes the methods involved in the development of the design tool envisioned for this thesis. This chapter includes an investigation of space filling volumes, print related input parameters and the description of the vector-based print path modelling in the digital design environment. The chapter also describes how the performance estimations are implemented in the design tool.

The fourth chapter gives a short summary of the printing process and material used to assess the feasibility of the development in a physical experiment.

The fifth chapter presents the results of the application of the developed design tool and experimental printing of two demonstrator objects.

The sixth and last chapter summarizes the bespoke and discusses the developed technology in the context of sustainable construction.

2. Fundamentals

2.1. State of the Art in building scale Additive Manufacturing

The history of additive manufacturing with cement-based materials starts around 1997 when Joseph Pegna reports of his first attempts in developing a solid freeform construction method. This first attempt uses a modification of the classical powder bed binder jetting (3DP) process (Sachs et al., 1993). It is based on selective binding of sand layers with cement as binder (Pegna, 1997). The only exception of modern 3D concrete printing processes still using a powder bed approach is the D-Shape process by Cesaretti and Dini (2014).

Recent concrete printing processes are mostly based on classical Fused Deposition Modeling (FDM) (Crump, 1992). In the 3D concrete printing modification of this process, a fresh cement mortar is extruded at a printer head as a continuous filament and placed via a 3D positioning system. Most processes use either a gantry-based system or a multi axis industrial robot.

As the developments in this work are specifically targeted to extrusion based additive manufacturing, the following section focuses on this fabrication method. An overview of relevant projects and their main characteristics is given in Table 1 below.

Table 1: Early pioneers, commercial implementations and newer research in extrusion based additive manufacturing with concrete

	Reference	Keyword	Path calculation	Internal structure
Early pioneers	(Khoshnevis and Dutton, 1998)	Contour crafting	CNC software	Zigzag
	(Lim et al., 2011)	Concrete Printing	Slicing	Circular vertical voids
Newer research	(Gosselin et al., 2016)	Freeform UHCP extrusion	Continuous	3D sinus wave
	(Näther et al., 2017)	ConPrint3D	Slicing	none
	(Henke, Talke and Winter, 2017)	Lightweight Concrete Printing	Continuous	Vertically open voids
Commercial implementations	(WinSun3D, 2019)	Several 3D printed houses, also multistory	Unknown	Zigzag
	(Apis Cor, 2019)	On site 3D printing	Unknown	Zigzag
	(XtreeE, 2016)	3D printed post in Aix-en-Provence	Continuous	Doubly corrugated sinusoidal shell

2.1.1. Early pioneers of 3D concrete printing

Among the extrusion based concrete printing processes, the following two stand out as the pioneering projects:

One of the first fully automated processes is the Contour Crafting method developed at University of Southern California (Khoshnevis and Dutton, 1998). Khoshnevis initially developed this method independently of a specific material but focused on concrete printing later (Khoshnevis and Bekey, 2002). In this process, concrete is extruded through a nozzle and accompanied by a trowel for surface smoothing. The printed contours can be regarded as a lost formwork and thus replace the traditional formwork. A later development even features multiple nozzles for contours and filling as well as a controllable trowel for smoothing of curved contours (Khoshnevis, 2004). By extruding two filaments simultaneously it is possible to create the inner and outer contour of a wall at the same time. A zigzag like internal support structure stabilizes the two contours. Afterwards they can be filled completely with concrete. Figure 1 shows a contour crafted straight wall with solid infill on the left and a more complex curved wall with zigzag infill on the right.
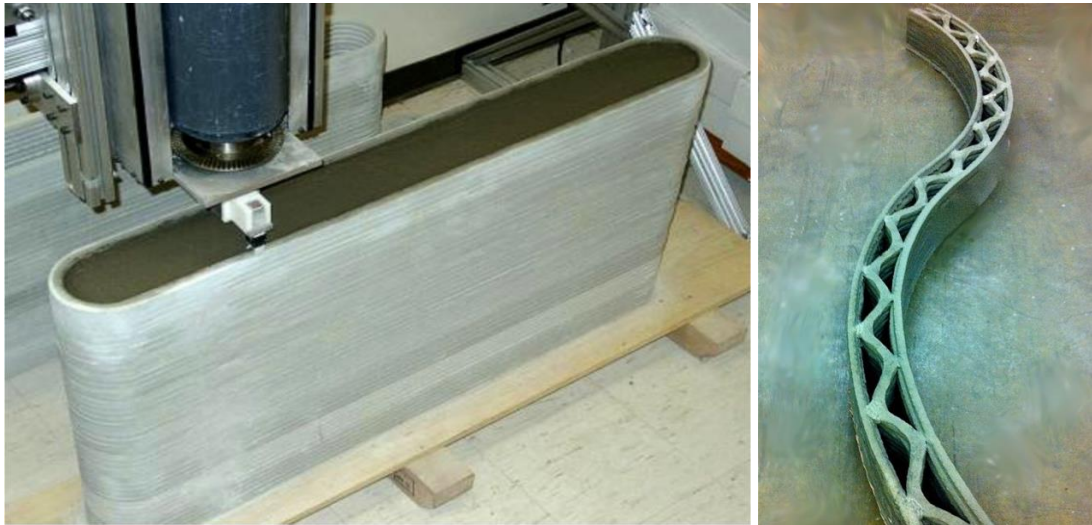
Figure 1: Early demonstrator of a Contour crafted wall with solid infill (left) and Contour Crafted wall with zigzag infill (right) (Khoshnevis et al., 2006)

The large-scale demonstrators produced in this project are straight or single corrugated. In the vertical plane they are limited to be vertically straight and thus do not include any overhanging features. Khosnevis envisioned a variety of functions to be implemented during the printing process including overhanging dome like roofs, automated steel re-inforcement, plumbing, electrical installation, and tiling. To date however, these func-tions never left the state of a vision towards an actual implementation of the concept. (Khoshnevis, 2004)

The second pioneering project is the 'Concrete Printing' process developed by Lim et al. at Loughborough University (2009). A gantry-based frame mounted robotic system with relatively large dimensions of roughly 5.0 meters in length, width and height posi-tions the printer head in space. The fresh concrete mortar is pumped to a nozzle where it is extruded as continuous filament layer by layer. The nozzle diameter is 9 millimeters to ensure a reasonable print resolution. Within the same project, Le et al. conducted extensive research regarding the material properties to enable pumping and extruding of the concrete (2012). These main material properties are described in detail later in paragraph 2.3. The feasibility of the process is shown with the so called 'Wonderbench' demonstrator pictured in Figure 2 below (Lim et al., 2011). This is a multifunctional wall like element including several added functions: Internal vertical voids reduce the density of the element and can be utilized for plumbing. The sizes of the voids are adapted to the shape of the element. The voids are also used to place post tensioned reinforce-ment.

The shape is a convex and concave curve to demonstrate the design freedom that comes with the technology of 3D printing (Lim et al., 2011).
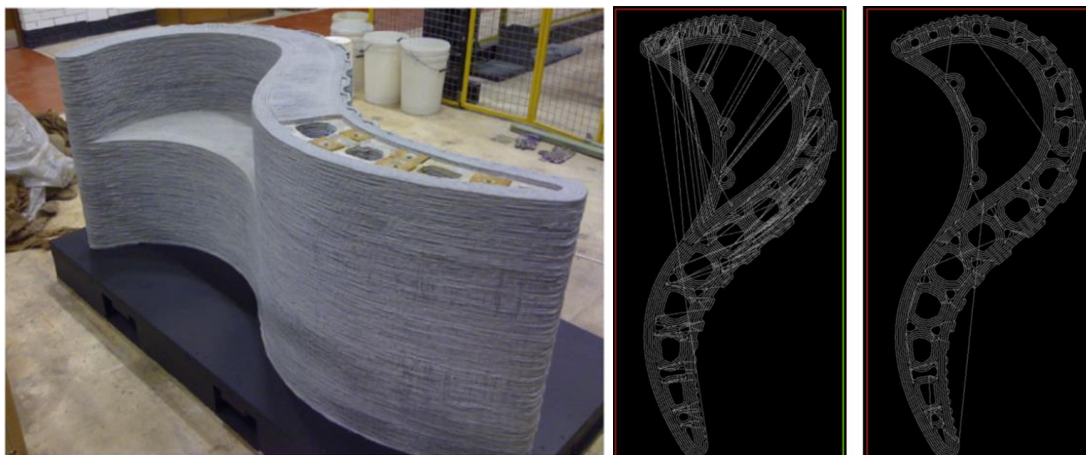

Figure 2: Wonderbench demonstrator with internal voids printed at Loughborough University (left) (Lim et al., 2012, p.263) and Wonderbench print paths before and after optimization (right) (Lim et al., 2012, p.265)

Lim et al. report that they use commercial slicing and CNC machining software to generate the print paths from a 3D model. As this software is not optimized for 3D printing and certainly not for 3D concrete printing, the resulting print paths are not continuous and include many on and off operations. To post optimize the print paths, Lim et al. developed an optimization script which links adjacent start and end points of paths to reduce the overall start and stop operations in the printing process. A before and after comparison of non-optimized and optimized print paths is shown in Figure 2 above. By making the printing process more continuous, savings on build time of up to 30% were achieved (Lim et al., 2012, p.265).

2.1.2. Newer research in extrusion based concrete printing

At the University 'Nationale Supérieure d'Architecture Paris-Malaquais' Gosselin et al. developed a new 3D concrete printing process based on Ultra-High-Performance-Concrete (UHCP) extrusion. The outstanding of this research project is the demonstrated ability to print complex geometry and overhangs without the need for temporary support structures. The large demonstrator shown in Figure 3 below features a curved shape, overhanging features and a complex internal structure. The project is embedded in the architectural context of unconstrained design freedom in rehabilitation projects.
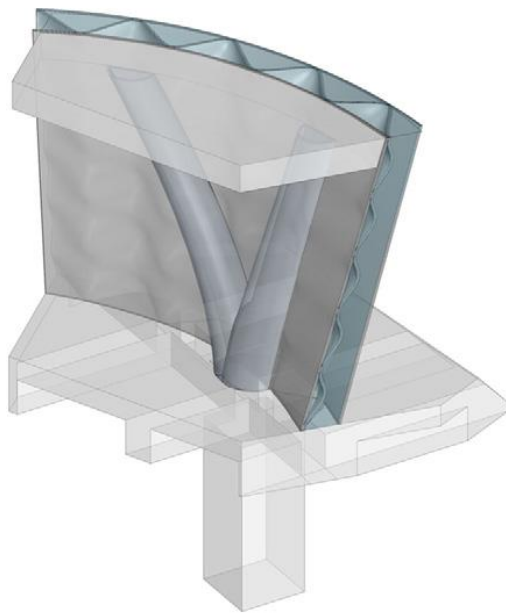
Figure 3: 3D model of multifunctional wall (left) and printed demonstrator object with detail of internal wall structure (right) (Gosselin et al., 2016, p.106)

The internal structure shown in the bottom right of Figure 3 above is a three dimensional double-corrugated surface defined by two sinus waves. This so called 'bi-sinusoidal shell' (Gosselin et al., 2016, p.105) resembles an egg box or double corrugated cardboard and reduces the contact points between inner and outer shell while maintaining a structural functionality as well. The small number of contact points limits the heat transfer trough the wall by reducing the overall cross section of thermal bridging concrete. To work as an insulating element, Gosselin et al. report that the thermal performance could be further enhanced by filling the internal voids with a foam like insulation material.

In contrast to the pioneering 3D concrete printing projects mentioned early in this chapter, this project is fully embedded in the parametric design environment Rhino and Grasshopper (McNeel & Associates, 2019). This setup gives full control over the print paths created from the 3D model and the 6-axis industrial robot used for printing. The so called 'tangential continuity method' (Gosselin et al., 2016, p.103) exemplifies the potential that can be obtained from advanced design tools. Locally decreasing thickness of the printed layers in areas of larger overhangs yields non-planar layers with increased contact areas between filaments. The benefit is an increased potential to print overhangs with better stability. In addition, planning the print path as a single continuous path reduces print time and guarantees and uninterrupted concrete flow (Gosselin et al.,

2016). Gosselin et al. also show a wall element with different hole geometries intended as sound absorbing cells. The cells shown in Figure 4 below could provide an acoustic functionality to a wall element.

In another study conducted at Loughborough University, Buswell et al. add functionality to 3D printed wall elements by enhancing their thermal insulation performance. They compare two 3D printed thermally enhanced gypsum panels. Although the panels were printed in gypsum, not concrete, the results of the geometric optimization can be transferred to concrete as well. The thermal conductivity of both panels was evaluated in a hot plate testing device. When comparing the results of the panels pictured in Figure 4 below, the results show a nearly halved conductivity for the left panel compared to the right panel (Buswell et al., 2007, p.230). This is not only due to the reduced bulk density but also due to a reduced number of conductive thermal bridges in the panel.
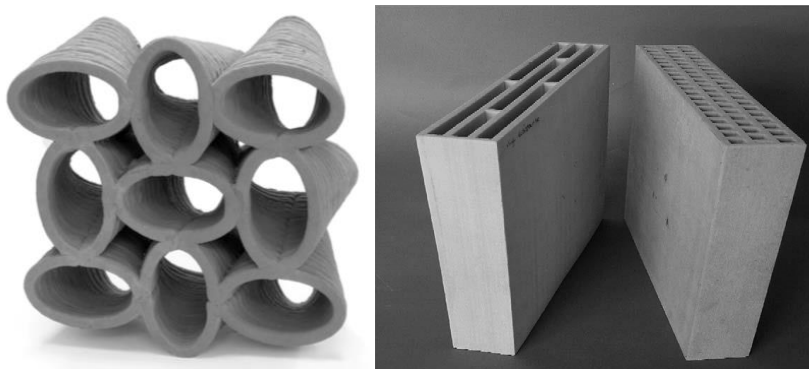

Figure 4: 3D concrete printed acoustic damping wall element (Gosselin et al., 2016, p.107)(left) and 3D printed gypsum elements (right). Left element: 0.112 W/mK, right element: Nearly double of left panel (Buswell et al., 2007, p.230)

'CONPrint3D' is a new printing process developed by Näther et al. at Technical University of Dresden (2017). The idea of this project is to use conventional construction machinery for on-site (in-situ) concrete printing. Particularly, a mobile truck mounted concrete pumping crane is used as the robotic manipulator for filament placement. The crane is software calibrated to compensate crane movement and achieve sufficient accuracy. The method uses extrusion as primary additive manufacturing principle but couples the nozzle with moving temporary formwork like the trowels in the Contour Crafting process. Instead of printing several adjacent filaments with optimal voids in between them, a massive single filament with a width greater than 10 centimeters is extruded (Näther et al., 2017). As such, the process is neither appropriate for printing overhanging features nor smaller scale internal structures.

Cesaretti et al. developed a printing process to be applied in vacuum conditions such as on the Moon. The process is based on powder bed printing but as the vacuum makes the powder bed obsolete, the process can neither be characterized as classical selective binding nor as classical extrusion. This project conceptualizes an internal cell structure inside the shell of a dome like structure. The shell is supposed to protect inhabitants from the harsh environment in space. The internal structure pictured in Figure 5 is foam like and thus contains closed cells for optimized stability and thermal insulation (Cesaretti et al., 2014).
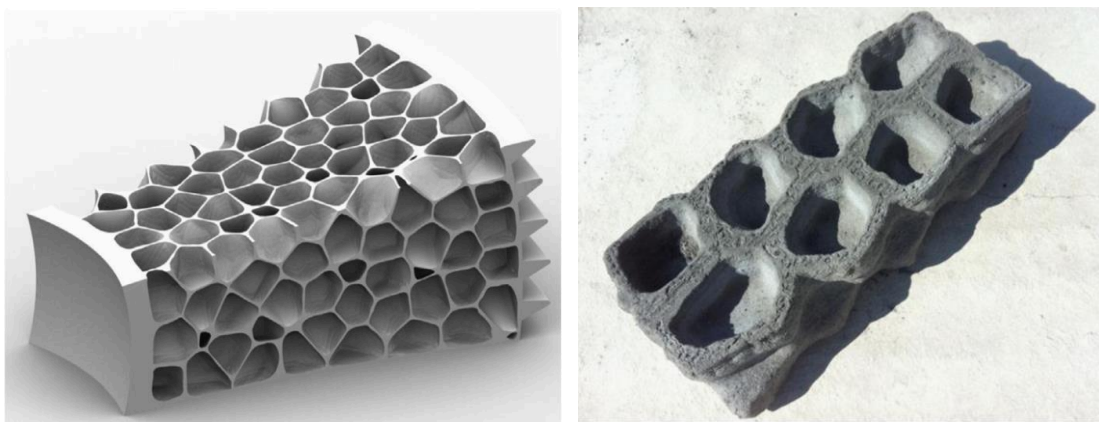

Figure 5: CAD drawing of foam like cell structure (left) and test print of cell structure (right) (Cesaretti et al., 2014, p.435;447)

At the Technical University of Munich, Henke et al. develop a novel printing process based on lightweight concrete. Compared to conventional concrete, lightweight concrete contains lightweight aggregates instead of rocks and sand. According to DIN EN 206:2017-01, lightweight concrete has a density of 800 kg/m^3 to 2000 kg/m^3. In contrast, the density of conventional concrete is in between 2000 kg/m^3 and 2600 kg/m^3 (DIN EN 206:2017-1, 2017). Several materials such as expanded slate, glass, clay, or pumice can be used as aggregates.

The concrete mixture applied by Henke et al. contains either wood chips or expanded glass granulate as the lightweight aggregate. Due to their low thermal conductivity, lightweight concretes can combine load bearing and insulating features in a single material. In addition, the low weight of the concrete is expected to allow the printing of relatively large overhangs (Henke, Talke and Winter, 2017, p.8). With the ability to exceed the limits of only vertical layering, a higher degree of geometrical freedom may be achieved. This freedom could be used to print air cavities inside concrete elements to further improve the thermal conductivity of 3D printed lightweight concrete elements.

Figure 6 (left) shows a 3D printed wood based lightweight concrete test object showing an overhang of 26%. Figure 6 (right) shows an internal structure of vertically open internal cells. The cells are supposed to further increase the thermal performance of printed elements and allow easy installation of wiring and plumping.

Figure 6: 3D printed wood based lightweight concrete test object showing an overhang of 26% (left) and lightweight concrete test object with internal voids (right) (Henke, Talke and Winter, 2017)

As the work of Henke et al. is the foundation for the development in this thesis, the process is described in detail in paragraph 4.

2.1.3. Commercial implementations of concrete printing

Ever since Khoshnevis and Lim et al. first introduced their Contour Crafting and Concrete Printing technologies, commercial adaptations of large-scale 3D printing spread dynamically in the building industry. The list of companies experimenting in the field is growing rapidly (Woensel et al., 2018). As a complete market overview would already be outdated once it is written, only a few examples are described in the following:

The Shanghai based company Winsun China, whose official name is Yingchuang Building Technique Co Ltd., is the first company to commercialize a full 3D printing process for the scale of entire houses. With several completed large-scale fully printed projects, such as 10 basic houses printed in 24 hours or an office building in Dubai, the company made headlines in the news (3DPrint.com, 2016; Süddeutsche Zeitung, 2017).

The 3D printing process used is similar to the Contour Crafting method described in the chapter 2.1.1 'Early pioneers of 3D concrete printing' above. A fresh concrete mortar is pumped through a hose and extruded trough a nozzle moved by a large portal frame printer. The printer is applied to prefabricate elements which are then transported to site and assembled via classical methods. Winsun claims it is using recycled materials from

construction and industrial waste for its concrete mixture (South China Morning Post, 2017). Details about the materials used are not published.

Figure 7: Offsite extrusion-based printing of concrete elements with internal zigzag structure (left) and 3D printed villa on the WinSun company property (right) (WinSun3D, 2020)

As pictured in Figure 7 above, Winsun prints an internal zigzag structure inside their elements for stabilization, insulation and to generate installation space. Details about the performance of the structure have not been published. For their multi story buildings they also put steel reinforcement into the voids and fill them with poured concrete to achieve a statically resilient construction (WinSun3D, 2019). The villa pictured in Figure 7 (right) above was printed by WinSun in 2005 and is located on the property of the company. Surprisingly, only the vertical outside and inside walls were 3D printed. The ornamental elements like balconies, window frames and pillars were produced conventionally (Ankenbrand, 2015). This suggests that only standard vertical elements without overhangs can be printed with Winsun's technology. One can conclude that the full potential of the 3D printing technology is thus not fully exploited in this project. The company puts its focus on speed and cost instead. In early 2020 WinSun claimed, it printed 15 little isolation houses for doctors and medical staff involved in the fight against the Corona virus in under 2 hours per house (WinSun3D, 2020)

Apis Cor is a 3D printing company based in the United States and known for its unique circular 3D printer. Unlike the WinSun printer or other examples, the Apis Cor printer is installed directly on site (in-situ).

Figure 8 below shows a 640 m^2 large administrative building printed in Dubai in 2019. The building features round walls to showcase the potential of the 3D printing technology. Corrugated or overhanging elements however have not been implemented.

A zigzag pattern, like the vertically open cell pattern found in WinSuns or Khoshnevis projects, can be observed inside the walls.
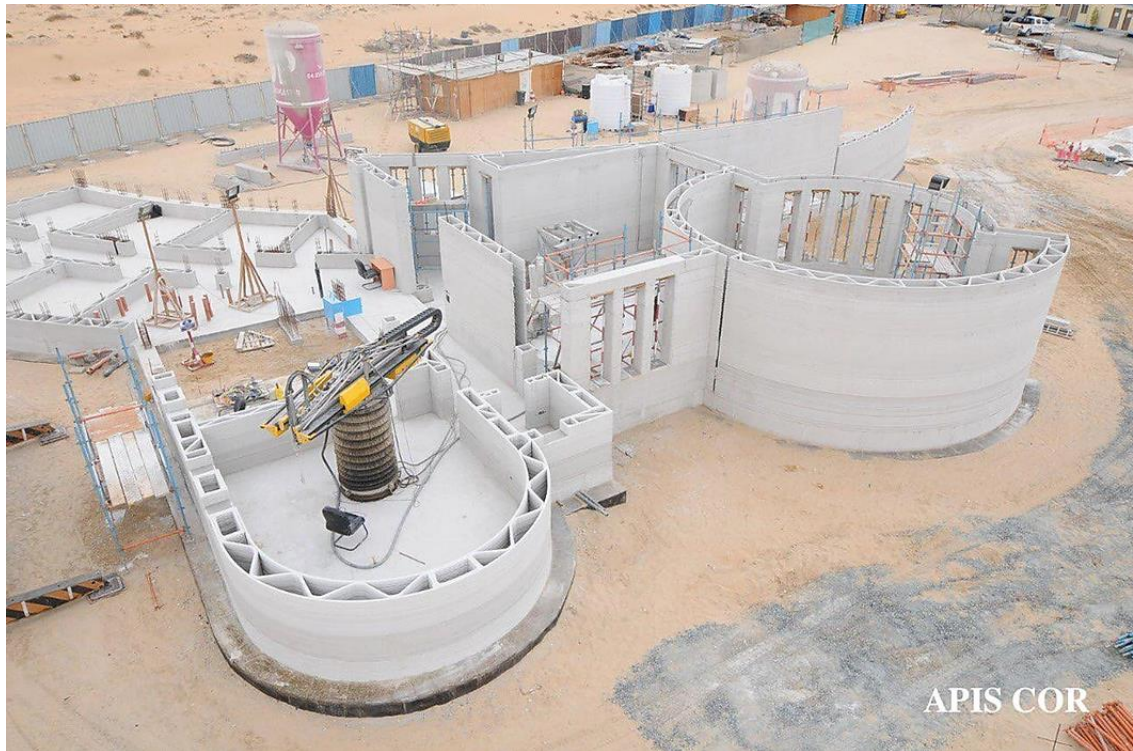

Figure 8: Two story administrative building in Dubai printed by Apis Cor in 2019 (Apis Cor, 2019)

XTreeE is a company founded as a spin-off based on the developments of Gosselin et al mentioned in the section 2.1.2 above. The process is based on UHCP extrusion and uses a 6-axis robot for filament placement. The company is specialized in printing complex freeform geometries rather than simple geometries seen in other projects. Figure 9 below shows a wall demonstrator with sinusoidal outer shell and a double corrugated internal structure similar to the structure printed inside the wall element by Gosselin et al.

Figure 9: Sinusoidal wall with internal 3D sinusoidal shell printed by XTreeE (left) and post for a school in Aix en Provence printed with temporary supports and as lost formwork (left) (XtreeE, 2016)

The pillar pictured in Figure 9 above was printed for a school in Aix-en-Provence in France and demonstrates the degree of geometrical freedom conceived through 3D concrete printing technology. Nevertheless, the process still involves manufacturing constraints and thus has to be done in several steps. As the attainable overhangs are limited, temporary support structures had to be integrated in the prints. The pillar was printed in four parts which were used as lost formwork and got filled with concrete later (XtreeE, 2016).

2.1.4. Conclusion

Early pioneers and commercial implementations focus on printing mainly vertical wall elements with a zigzag pattern between an inner and an outer shell. Several functions can be integrated in the wall elements: The internal structure stabilizes the prints and forms voids that could be used for thermal insulation and installation pipes or wires. All examples described in this chapter include vertically open cell structures, if they include any internal voids. Cesaretti et al. show the only example of a closed cell structure, but their printing process works only under vacuum conditions. Little is known about the actual thermal performance of the walls but the fact that the voids are either filled with

foam or left empty, such as in the projects built in the hot climate of Dubai, suggests that the sole insulation performance of current wall designs is insufficient. To function as a mono material construction, the performance has to be further improved.

The digital design workflow from 3D model to print path calculation is based on conventional slicing operations in most of the projects. Lim et al. use a post optimization script for a reduction of printing interruptions in their conventionally sliced print paths (Lim et al., 2012). Only a few pioneering projects such as Gosselin et al. try to optimize their print paths specifically for large scale concrete printing.

The research of Gosselin et al. showcases the benefits of fully parametric print path planning opposed to classical slicing operations. The multifunctional wall element produced as a demonstrator object could be printed with only one continuous print path (Gosselin et al., 2016). In addition, a greater degree of geometrical freedom with corrugated surfaces and overhangs could be used to produce a wall demonstrator with multiple functions.

2.2. Cell structures

2.2.1. Cell structures in additive manufacturing

Cell structures are a widely spread phenomenon in natural materials like wood, bone tissue, cork or beehive honeycombs (Nachtigall and Wisser, 2013, pp.76–79). These cellular materials offer exceptional functional properties like high stiffness and strength, low weight, or reduced heat transfer. Logically they have thus already been mimicked in engineered materials and can also be found in construction materials like insulation foam.

Cell structures can be categorized into open and closed cells. Whereas closed cell structures can only be made of three-dimensional cell configurations, open cells can be composited of both two-dimensional and three-dimensional cell arrangements. An example for a two-dimensional open cell configuration is the classical two-dimensional honeycomb. Seen from an additive manufacturing perspective it can be produced with the same print path in every layer. Closed cell structures consist of complex polyhedral cells. Cells of closed cell structures are not interconnected to each other. They can be arranged both regular and irregular. (Mazur et al., 2017, p.119)

Additive manufacturing processes provide the opportunity to produce cellular structures with custom properties (Ajdari et al., 2012). Complex open cell structures can be printed both in particle bed and extrusion-based printers.

Closed cells, however, can only be printed in extrusion-based processes. In particle-based processes, the supporting particles would remain inside the cells after printing. Applications of 3D printed cell structures can, for example, be found in 3D metal printing or custom fit bone tissue printing (Markforged, 2020; Pandithevan and Gurunathan, 2009). These structures have in common that they were created with high precision small scale printers using special fast hardening filaments.

To date, cell structures in building scale additive manufacturing with concrete are realized as open cells or simple 2D honeycomb structures for the sake of stabilization and insulation. A simple zigzag pattern can be observed in many projects such as in the pioneering work at Loughborough University or commercial implementations of WinSun and Apis Cor (Apis Cor, 2019; Lim et al., 2009; WinSun3D, 2019). Henke et al. realized several demonstrator objects with 2D honeycomb infills using lightweight concrete at the Technical University of Munich. Closed cell structures, however, have not yet been reported to be used in building scale additive manufacturing with concrete.

2.2.2. Theory of heat transfer in air cavities

As a resting gas, air has a low thermal conductivity. This property makes encapsulated air the basis for many insulation processes. But, when air leaves its resting state, convection is the process transferring heat. Convection accelerates the heat transfer and causes a loss of the insulating property of the air (Bankvall, 1972).

Buoyancy is the physical effect driving natural convection. It is the movement of air caused by temperature differences. In an air cavity, convection is induced by differently tempered boundary surfaces. In a porous material, the temperature difference between the sides of an element can be distributed to many internal surfaces leading to lower temperature differences between adjacent surfaces (Bankvall, 1972). A lack of space in a closed cell can additionally prevent convection induced circulating air.

By decreasing the encapsulated air volume, the likelihood for convection inside an air-filled cell can thus be reduced (Bankvall, 1972). Figure 10 below shows the three modes of heat transfer as well as the total heat transfer through a closed air cavity studied by Bekkouche et al. Conduction (blue line) and convection (green line) show opposing

developments: The conduction decreases with increasing air layer thickness whereas convection increases. Almost no convection occures in cavities smaller than 40 mm.

The radiation (red line) is not affected by the air layer thickness. This is because the inside surface area of the air cavity is assumed to be constant. Reducing the surface area to volume ratio could however reduce the radiation (Bekkouche et al., 2013). Looking at the total heat transfer (black line), an ideal cell size of around 40 – 60 mm can be identified.
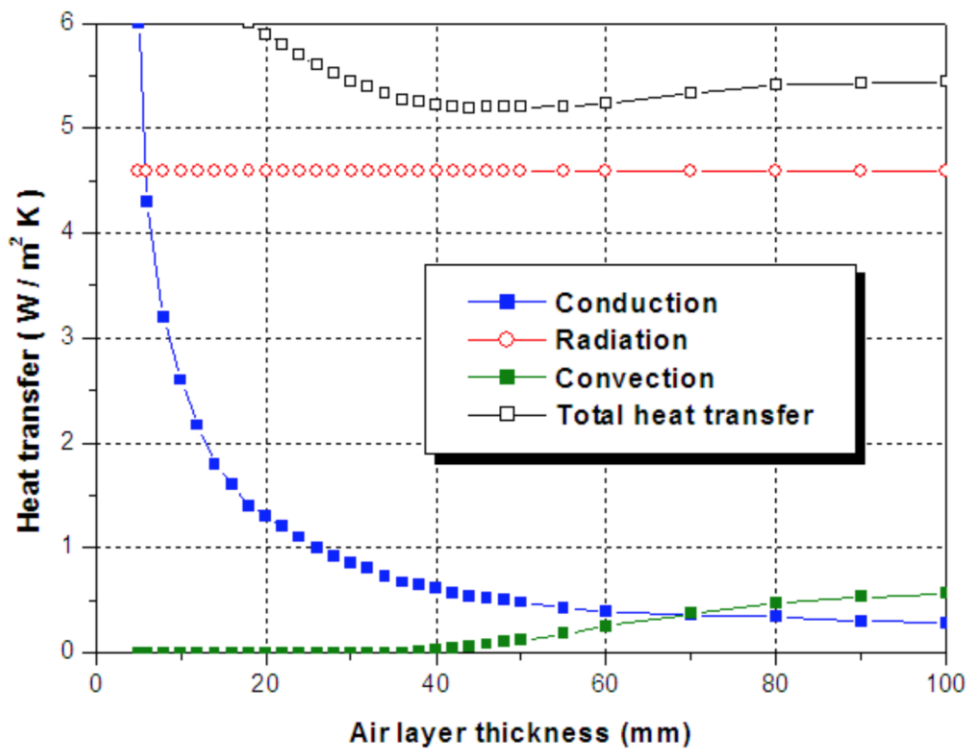
Figure 10: Estimated heat transfer in a closed air cavity bounded by ordinary materials e = 0.9 (Graphic from Bekkouche et al., 2013)

Information on how to estimate the heat transfer in air filled cavities can also be found in building standards. DIN EN ISO 6946 defines the heat transfer coefficient of a building element as the U-Value [W/m²K]. It is calculated as the reciprocal of a sum of heat transfer resistances. The heat transfer resistances of layers in a construction are calculated based on their thickness $d\ [m]$ and thermal conductivity $\lambda\ [W/mK]$ as:

$$U = \frac{1}{R_t} = \frac{1}{R_{si} + \frac{d_1}{\lambda_1} + \frac{d_n}{\lambda_n} + \cdots + R_{se}} \tag{2.1}$$

The heat transfer resistance for airflow on the inside and outside surface of a horizontal building element are R_{si} = 0,13 m²K/W and R_{se} 0,04 m²K/W (DIN EN ISO 6946, Table 7). Table 2 lists heat transfer coefficients of air cavities of different thicknesses.

Table 2: Heat transfer resistances and coefficients in layers of resting air. Adopted from DIN EN ISO 6946:2018

Air layer thickness	[mm]	5	7	10	15	25	50	100	300
Heat transfer resistance	[m²K/W]	0,11	0,13	0,15	0,16	0,18	0,18	0,18	0,18
Heat transfer coefficient	[m²K/W]	9,09	7,69	6,67	6,25	5,56	5,56	5,56	5,56

In building elements with inhomogeneous layers such as in wood frame constructions or cellular structures, the total heat transfer coefficient can be approximated by calculating the respective proportions of the materials in the construction (DIN EN ISO 6946, 2018). The average U-value $U_{average}$ based on the areas of the materials $A_n \ [m^2]$ is calculated as:

$$U_{average} = \frac{U_1 \cdot A_1 + U_2 \cdot A_2 + \cdots}{A_1 + A_2 + \ldots}$$

(2.2)

2.2.3. Space filling volumes

Space filling volumes can tesselate space entirely. They can be regarded as the geometric representation of closed foam materials. As they do not leave any gaps in between each other, they can fill space homogeneously. This homogenous behavior of space filling volumes can be utilized to produce closed cell structures for wall elements with enhanced thermal characteristics.

Geometrically, there is only a limited number of space filling geometries. Amongst the convex polyhedra, there are only five main geometries with the ability to tesselate space entirely only by arraying them in space.

The five geometries are the cube, prism, rhombic dodecahedron, elongated dodecahedron and truncated octahedron pictured in Figure 11 below. (Wells, 1991, pp.233–243)
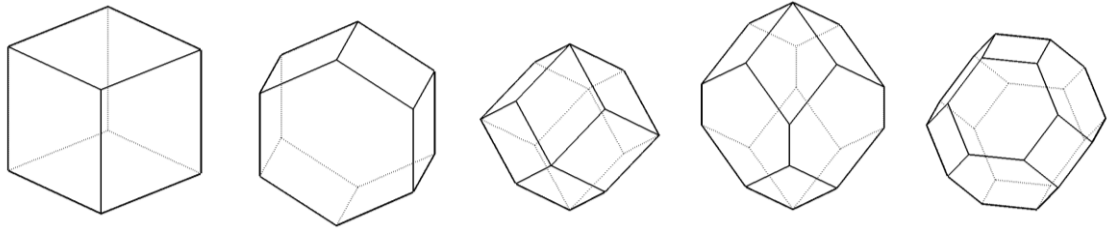
Figure 11: The five main space filling polyhedra. From left to right: Cube, Prism, Rhombic Dodecahedron, Elongated Dodecahedron and Truncated Octahedron (Graphic created by the author)

Table 3: Space filling volumes and their number of faces and surface area to volume ratio at unit volume of 1 m³

	Cube	Prism	Rhombic Dodecahedron	Elongated Dodecahedron	Truncated Octahedron
Surface area to volume ratio	6.0 m²/m³	5,746 m²/m³	5,35 m²/m³	5,493 m²/m³	5,315 m²/m³
Number of faces	6	8	12	12	14

They all feature several symmetries and are composed of a limited amount of different face types. Opposing faces are always congruent. These symmetries and regularity help to reproduce these shapes in computational engineering (Réti et al., 2020, p.2).

Even though all these shapes can tesselate space, they are not equally suitable for 3D printing thermally enhanced cell structures. As commonly known, a high volume to low surface area is advantageous for limiting heat losses. The ideal geometric shape in this regard is the sphere. Independently of its size, it includes the highest possible volume with the least surrounding surface. Table 3 shows the five main space filling volumes and their number of faces and surface area to volume ratio at unit volume of one cubic meter.

Of all the space filling shapes mentioned above, the truncated octahedron is composited of the highest number of faces. With its 14 faces, the truncated octahedron is the shape which adapts closest to the ideal shape of the sphere. The surface area of a truncated octahedron with edge length a is $S = \left(6 + 12\sqrt{3}\right) a^2$.

The respective volume is $V = 8\sqrt{2}\, a^2$. The surface area to volume ratio of a truncated octahedron with unit volume one is thus $5{,}315$. It is thus in between the ideal ratio of a sphere with $4{,}835$ and a cube with $6{,}0$. (Weisstein, 2017)

2.3. Concrete extrusion process parameters and constraints

2.3.1. Layer cycle time

The development of this work is based on extrusion-based 3D concrete printing. Concrete mixtures used in extrusion-based additive manufacturing must balance two main contrasting properties: On the one hand, the concrete must be liquid enough to be pumpable and keep its pumpability until it is extruded. On the other hand, to support following layers, the fresh concrete needs to harden and build up strength as quick as possible once it is extruded.

Consequently, when modelling the print path, a variety of material and process related parameters should be considered. The key material properties like pumpability, extrudability and buildability were first described and investigated by Le et al (2012).

Extrudability can be described as the ability to push a viscous material such as concrete through a nozzle, where it is extruded as a continuous filament and then hardens more or less in the cross-section of the nozzle (Le et al., 2012).

The term 'buildability' describes the ability of the extruded concrete to support following layers. It can be quantified as 'the number of filament layers which could be built up without noticeable deformation of lower layers' (Le et al., 2012). Matthäus et al. use the term 'green strength' to describe the initial stability of the concrete to stay true to its extrusion shape. Buildability is influenced by the age of the filament, aggregate mixture and cement proportion as well as additives like accelerators or retarders.

All these properties depend on the open time of the fresh concrete. Timing is hence a major issue in 3D concrete printing processes. In the context of additive manufacturing, open time is the period in which the fresh concrete can be used for extrusion. The point in time at which hydration reduces the viscosity to a degree where it cannot be extruded anymore limits open time (Buswell et al., 2018).

For the actual design and print path generation, this results in the main parameter layer cycle time. The layer cycle time is defined by a lower and upper time limit. The buildability of the concrete mix defines the lower time limit. It determines the minimum delay before concrete can be placed in the same location on top of the previous layer (Buswell et al., 2018). The open time of the fresh concrete and the resulting bond strength between consecutive layers define the upper time limit. As reported by Buswell et al (2018),

too high cycle times may cause cold joints with weak or no bond strength between consecutive layers.

The ideal layer cycle time can be derived from the rheological concrete mix properties. Predicting it precisely and keeping it constant is however not easy. First, a consistent path length in every layer can be an easy measure to keep cycle times consistent. Geometrical freedom would however be limited. Secondly, changes of direction in the print path cause the robotic arm to slow down and thereby extend the cycle time. Cycle time can thus only be kept in a certain range. Predicting the exact cycle time before printing would enforce prior print simulation with dynamic robot movements.

2.3.2. Layer height

The layer height, meaning the vertical distance between consecutive layers, is not only defined by the nozzle size being used, but also dependent of the filament placement technique. The two main differences between the techniques are described below:

In a pressing process, the layer height is set slightly lower than the filament height. The filament extruded from the nozzle is hence slightly pressed onto the previous layer. Pressing the filaments onto each other can anticipate and thus prevent layer shrinkage (Bos et al., 2016, p.220). This process results in a high conformity of modelled and printed geometry since the height of every layer is almost equal. It is also advantageous for good interlayer adhesion and concrete compaction (Bos et al., 2016, p.220). Sloughing is the process used to produce the demonstrators in this work.

In a laying process, the layer height is set equal or slightly higher than the nozzle section width. This results in a smooth stacking of layers and avoids interaction between nozzle and filament (Bos et al., 2016, p.220). Setting the gap from filament to nozzle correctly, can help to achieve even surface finishes without the look of single filaments. However, due to compression of lower layers, the gap between nozzle and filament can increase during the printing process resulting in unpredictable differences in material deposition (Lim et al., 2009, p.9).

2.3.3. Overhangs

The possibility to produce overhanging features expands the overall geometric freedom of an additive manufacturing process since geometries can be designed beyond the limits of vertical filament placement. This greater degree of freedom allows the production of internal complex structures.

Especially internal closed cell structures make overhangs inevitable to close cells horizontally. If temporary support structures are not desired, overhangs are typically produced by cantilevering (Bos et al., 2016). Cantilevering can be provoked, when print paths are placed eccentrically above each other. As shown in Figure 12 below, the 2D offset of the print paths out of the filaments center of mass equals the distance consecutive filaments have to cantilever.

overhang in mm

Plane of cantilevering

center of gravity   *Underlying filament*

printpathwidth
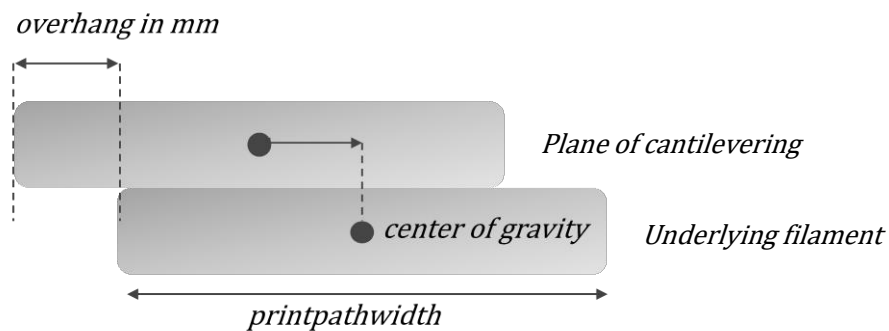
Figure 12: Definition of overhangs

Overhangs are dependent of the rheological properties of the concrete mixture used. The buildability, derived from the concrete's stiffness and strength determines, a filaments ability to cantilever (Le et al., 2012). As filament stiffness and strength increase over time, the ability to produce overhangs is process wise directly related to layer cycle time (Bos et al., 2016, p.218). Higher layer cycle times may thus improve the ability to print overhangs. Nevertheless, balancing overall printing speed, overhangs and required layer to layer adhesion limit layer cycle time.

Overhangs are limited not only by the rheological properties of the concrete mixture used, but also by the general 3D context and global overhang they occur in. Both, the filaments in the plane of cantilevering and underlying filaments influence overhangs.

Underlying layers support the load on the filaments caused by the eccentrical placement of following layers. This support capacity is related to the respective compression strength of the filaments (Bos et al., 2016, p.219). The tensile strength of the filaments in the plane of cantilevering defines, to what degree they can cantilever before they collapse due to tearing. Bos et al report that 'the mass available in the plane of cantilevering positively influences the maximum angle of cantilevering' (2016, p.219). Limiting the global size of overhanging features and leaving enough supporting counterweight can thus stabilize cantilevering structures. Gosselin et al report that corrugated and

undulating structures are a proven concept to efficiently enhance additively manufactured concrete geometries structurally (2016).

In a study of 3D printing lightweight concrete based on lightweight wood aggregates, Henke et al. could achieve overhangs of up to 26% at a filament width of 10 mm (2016, p.8). The overhang of 26% equals three millimeters of cantilevering. Using filaments of greater width might allow to scale up the degree of cantilevering.

3. Printpath modelling

3.1. Design tool concept

The review of State-of-the-Art concrete printing projects in section 2.1 above revealed that the computational workflow in the majority of the reviewed projects is based on conventional slicing operations. Even though this is a widespread and straightforward process, the optimization potential of manufacturing related issues such as continuity and overhangs in the print path is limited. To overcome these issues, more advanced control over the print path is necessary. Pioneering works, such as the developments of Gosselin et al., demonstrate the potential of parametric print path modelling in relation to production constraints and path optimization. In terms of path optimization, printing continuity is identified as major issue by Lim et al. (see chapter 2.1.1 above). Proceeding this context, the development of a design tool to plan continuous print paths is described in the following chapters.

Storing the control points of the print path in the actual printing order, can guarantee path continuity inherent in the system of design tool developed within this thesis. Paragraph 3.3. describes this procedure in detail.

The design tool is conceptualized to be aware of the production constraints in 3D concrete printing to ensure the printability of the designed geometries. In addition, the tool gives feedback about the performance and printability of the geometry. The user can thus improve the geometry in an iterative approach.

A wall element is the exemplary use case for the tool. The design tool is supposed to produce printable results with a minimum of user inputs. The so called 'user' could be an architect designing a wall element or a researcher conducting further research in the field of 3D printed cell structures. The main user inputs include:

Guide surfaces*:* Two guide surfaces define the shape of the wall element. These surfaces act as outer boundaries of the element and define its width, height, and length. Both surfaces can be straight, single, or double corrugated. In contrast to single corrugated surfaces unbending a double corrugated surface to a single flat plane is impossible. The user of the design tool can thus exploit a high degree of geometrical freedom.

Nevertheless, constraints like the largest possible overhang limit the shape of the guide surfaces. The user gets feedback about these constraints during the design process. Paragraph 3.9.1 of this chapter describes this feature.

Attractor point: Attractor points are a common concept in parametric design tools such as Grasshopper (Grashopper Primer V3.3, 2015). In the context of a multifunctional wall element, an attractor point may be introduced to vary the density of the cells inside the wall. The attractor point can represent special punctual loads or other user desired anomalies in the wall element. The graduation of the internal cell structure adds another layer of multifunctionality to the element as it could for example provide the function of a façade and column at the same time.

Cell shape: The shape of the cells inside the wall can be independently changed in their width, depth, and height. As changing cell sizes effect overhangs and estimated thermal conductivity, the design gives feedback regarding the effect of the changes made. This feature is described in paragraph 3.9 of this chapter. The sizes of the cells can also be variated and changed gradually as controlled by the attractor point.

Process parameters: Besides the above-mentioned geometrical inputs, several printing process related parameters and constraints are considered in the design tool. These include the basic print related inputs like layer height and filament width and in the feedback module also ideal layer cycle time and maximum overhangs. Detailed descriptions of these parameters are given in chapter 2.3 and the following paragraph 3.9. in this chapter.

See Appendix A for a detailed description of the design tool. A reference documentation of the implemented python Code is given in Appendix B.

3.2. Analysis of space filling arrays

The fundamentals of cell structures and space filling volumes are descibed in the paragraphs 2.2 of this thesis. Based on the review of space filling volumes, the truncated octahedron is selected as the geometrical foundation for the development of the closed cell structure in this work. The truncated octahedron shape is selected due to its low surface to volume ratio and small top and bottom surface. With its 14 faces, the truncated octahedron also adapts closely to the ideal shape of the sphere. Due to the limited overhangs being possible with the current extrusion process, the octahedron is

stretched vertically. Parametrically adjusting the stretch factor adjusts the geometry to a desired overhang angle.

Space filling arrays of truncated octahedron volumes are modeled as 3D Computer Aided Design (CAD) models to analyze their geometrical behavior. These 3D models are sliced into 2D layers just as in conventional 3D printing software. This "top-bottom" approach of conventional slicing software is applied to analyze the print paths which are necessary to print closed cell structures. The study of sliced print paths is used to investigate layer-to-layer transformations of the paths and to identify possible conflicts related to the printing process. A parametric print path generation will replace this "top-down" approach later. This approach is referred to as "bottom-up" approach throughout this thesis.
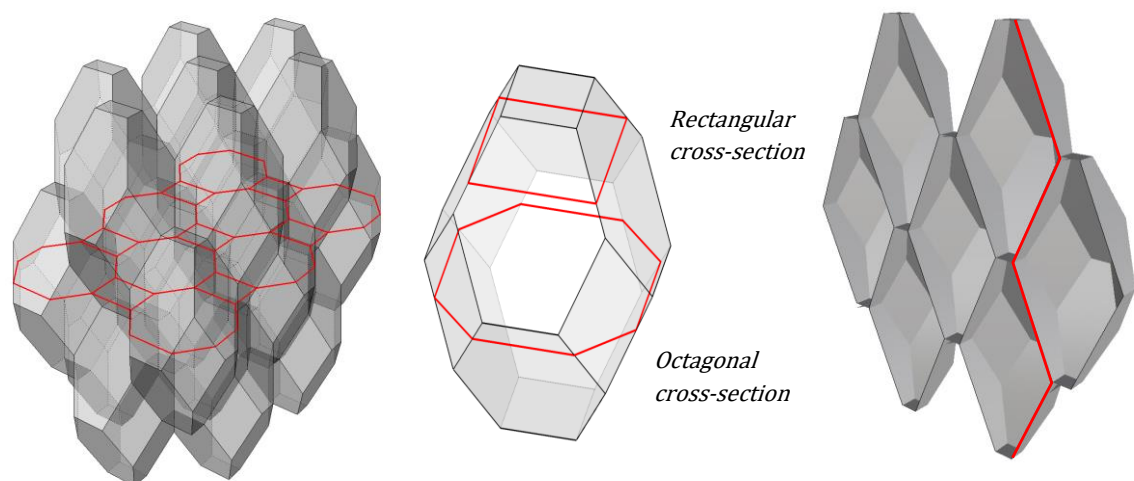
Figure 13: CAD model of space filling array of truncated octahedron shapes with exemplary print path slice (left), rectangular and octagonal cross section of truncated octahedron (middle) and vertical section with zigzag like contour line in red (right)

Depending on the slicing position in the octahedron volume, two different types of 2D shapes can be observed in Figure 13 above: The upper and lower part of the octahedron have a rectangular cross-section whereas the middle part has an octagonal cross-section. Neighboring cells are offset to each other by half a cell height in z direction. When the horizontal cross section of an arbitrary cell at half a cell height is an octagon with maximum size, the cross sections of neighboring cells are thus always rectangles at minimum size.

Looking at the layer-to-layer transformation of the horizontal cross sections, lines with equally increasing and decreasing lengths can be observed. The path lengths have

minimal and maximal lengths at which the direction in length development is reversed. The change in the length of the path segments is thus of periodic behavior. Figure 13 (right) shows a vertical section of cell array and the zigzag like contour of the cells in red. This zigzag shape is of periodic behavior as well.

3.3. Basic vector sequence

In classical FDM printing, direction parallel printing is a common pattern for dense, space filling infills (Jin et al., 2014). Referring to direction parallel printing as simple 'zigzag' or 'book reading pattern' is also possible. By adjusting start and end points of every layer to be identical, this pattern can be applied to print the whole geometry continuously.

The left side of Figure 14 below shows an arbitrary horizontal section of several truncated octahedrons arranged in a space filling array. The dotted line shows the conceptual approach of a continuous direction parallel print path. This concept is applied as the foundation for the following print path modelling.

A closer look at the 2D slices of the octahedron cells reveals that a continuous print path cannot be realized without doubling line segments. The problem is caused by the rectangular cross sections representing the neighboring cells of the octagonal cross sections. Printing the rectangles with an "in-out" movement in the print path solves this problem. An exemplary 2D slice of a cell array and its modification as continuous print path based on direction parallel printing is shown in Figure 14 below.
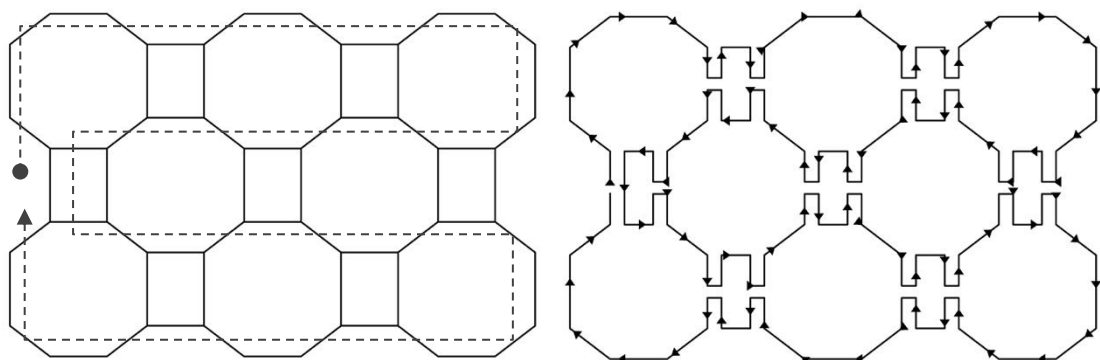
Figure 14: Exemplary 2D slice of a cell array with conceptual pattern of the print path (left) and an exemplary continuous print path the same slice (right)

The basic principle behind the print path modeling in this work is a sequence of several incremental vectors defining a print path vector sequence. The approach is inspired by

turtle graphics (Goldman, Schaefer and Ju, 2004). To create turtle graphics, an imaginary turtle, as representative of a point, is moved in a 2D plane with simple direction and distance commands relative to its current position. By taking the last calculated point of the print path as reference for the next point, path continuity can be coded inherent in the system.

The vector sequence describes the geometry of half a cell and thus the smallest repeating entity of the print path. The vectors are used to calculate the coordinates of control points on the print path. Figure 15 (left) below shows the basic vectors of a truncated octahedron print path. The full cell is built by mirroring the initial half-cell on a mirror line in the center of the cell (dashed line).
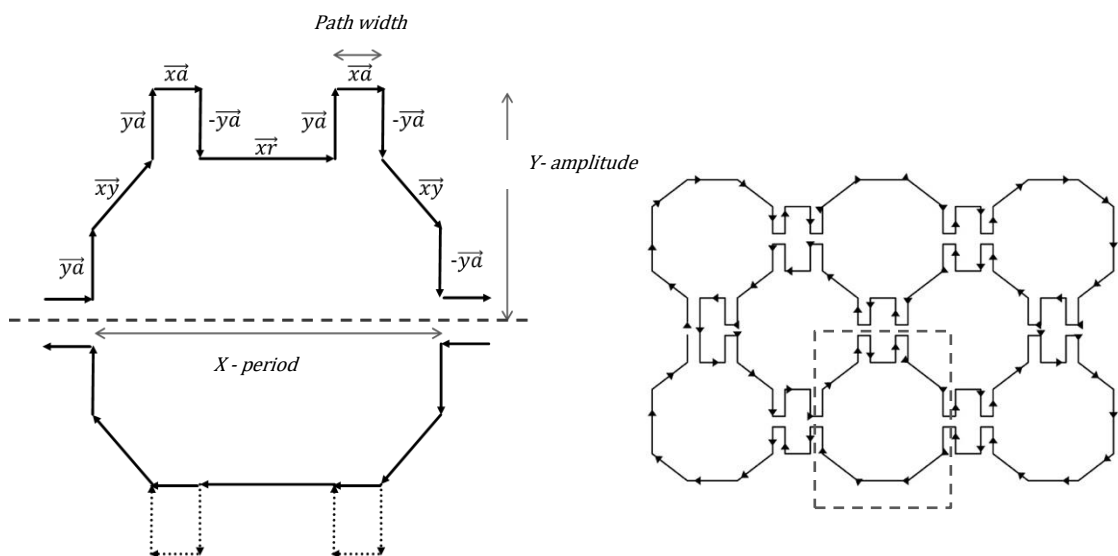
Figure 15: Exemplary clipping of vector sequence with incremental vectors and cell dimensions of truncated octahedron cell shape (left) and location of the clipping (dashed line) in a print path layer (right)

The vectors $\overrightarrow{ya}$, $\overrightarrow{xa}$ and $\overrightarrow{-ya}$ describe an "in and out" movement in the print path. This movement is necessary to guarantee the continuity of the print path. Together with the y coordinate of the vectors $\overrightarrow{xy}$ and $\overrightarrow{yx}$, these vectors also define the size of the cell in *y* direction (y-amplitude). The vectors $\overrightarrow{xr}$ together with the x coordinate of the vectors $\overrightarrow{xy}$ and $\overrightarrow{yx}$ define the size of the cell in x direction (x-period).

As the length of the vectors changes periodically from layer to layer, the print path can be calculated as a function of height.

A linearized sine function can describe the layer-to-layer transformation of the vectors defining the print path. The general formula of a linearized sine function (zigzag) is:

$$f(x) = \sin^{-1}(\cos x) \tag{3.1}$$

A zigzag function with an amplitude from 0.0 to a and a period p can be written as:

$$f(x) = \frac{a}{\pi} \cdot \sin^{-1}(\cos(\pi \frac{x-p}{p})) + \frac{a}{2} \tag{3.2}$$

As the segments of the print path increase and decrease in length at the same time, a secondary function describing the decreasing lengths is necessary. Phase shifting the original zigzag function reveals such a function for the decreasing segments. A phase shift of half a period can be achieved by simply negating the zigzag function:

$$f(x) = -\frac{a}{\pi} \cdot \sin^{-1}(\cos(\pi \frac{x-p}{p})) + \frac{a}{2} \tag{3.3}$$

For the vertical section, the period of the zigzag function translates directly to the height of the octahedron cell. The amplitude defines the width of the cell at its widest point. When x is defined as the height from zero to a desired height in a cell array, the zigzag function can be used to calculate the segment lengths of the print path for any given height. Any vector defined by the cartesian coordinates x, y, z can then be calculated as:

$$\vec{v} = (x, y, z) \cdot f(x) \tag{3.4}$$

As shown in Figure 13 above, the cross section of the truncated octahedron changes from an octagon to a square depending on the height of the section. The change of vector length is linked to the cross-section shape via the 1st derivative $f'(x)$ of the zigzag function. The derivative equals a zigzag function with doubled period:

$$f'(x) = \frac{a}{\pi} \cdot \sin^{-1}(\cos(\pi \frac{x-2p}{2p})) + \frac{a}{2} \tag{3.5}$$

This function defines the 'flipping point' that occurs in the print path when the octahedron cells change their cross-section shape. For $f'(x) < 0$, the shape is defined to be rectangular and for $f'(x) > 0$ octagonal.

3.4. Parametrizing print paths

The vector sequence described in the above paragraph is located in a fixed global co-ordinate system. It can thus only be used to calculate the print path of rectangular cell arrays with evenly sized cells. In a freeform wall element, as described by two guide surfaces, the internal cell structure needs to adapt to the given shape. At the scale of a single cell, the adaptation is done by variating the width (x) and depth (y) of the cell. Due to the fixed layer height and overhang constraints, the height (z) of the cells is fixed. The modeling process for calculating the print path based on two guide surfaces involves the following steps:

At first, boundary curves are derived from surface contour lines for every layer as shown on the left of Figure 16 below. Calculating the centerline between these two boundary curves is the next step. This centerline is regarded as the guide curve for the following modeling steps. The direction following the tangent of the guide curve is referred to as x-direction. The direction perpendicular to the tangent is referred to as y-direction.

Subdividing the guide curve in smaller partitions, defines the width (x) dimensions of the cells based on the segment length. To keep the space filling quality of the structure, the number of cells in both x and y direction is fixed for every layer. The following paragraph 3.5 describes the modelling of variable cell sizes in detail.

Figure 16 below shows two exemplary guidesurfaces on the left and the 2D drawing of boundary curves, centerline and divisions in x direction on the right. Based on the vector sequence, the cells are created inside the layer and division boundaries and along the centerline.
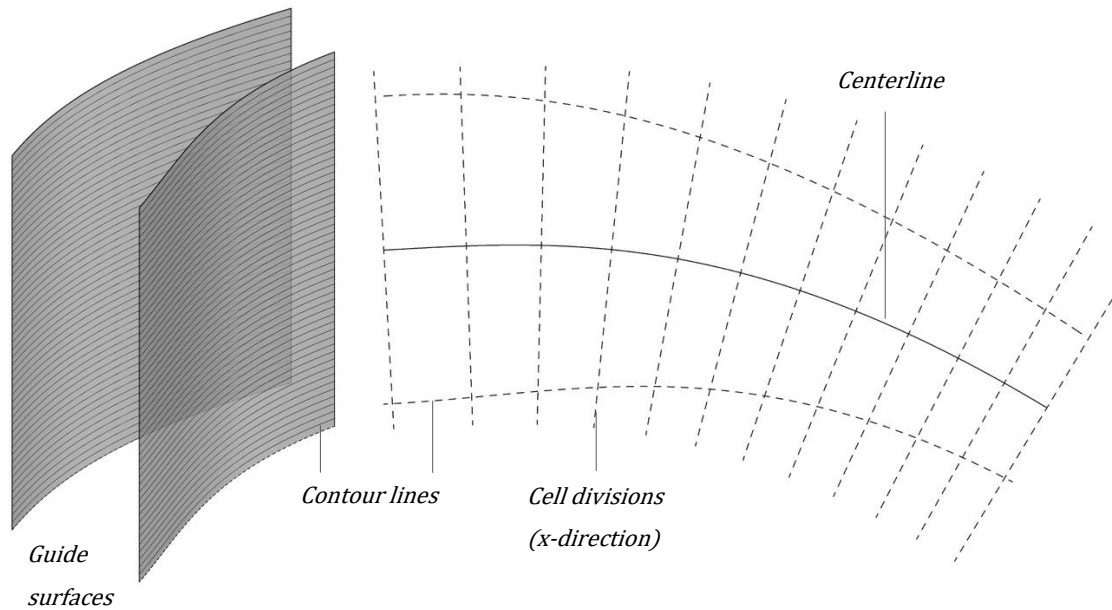
Figure 16: 3D model of guide surfaces with layer wise contours (left) and 2D drawing of contour lines, centerline and cell divisions in x direction

At the scale of a single cell print path section, the adaptation is carried out by reorienting the initial vector sequence in a local coordinate system. The reference for the reorientation is a guide curve which corresponds to the centerline between two boundary curves. Extracting the surfaces contour lines at a given height *z* yields these boundary curves.

The process of reorienting the vector sequence from the global coordinate system to a local coordinate system at a guide curve is shown in Figure 17 below. As drawn on the right-hand side of the figure below, the tangent at Point p is used as local *x* axis (u), while the normal at the same point is the local *y* axis (v). By calculating the angular difference (α) between global and local coordinate system, and rotating the vectors by that difference, the vector sequence can be reoriented in the new local coordinate system.
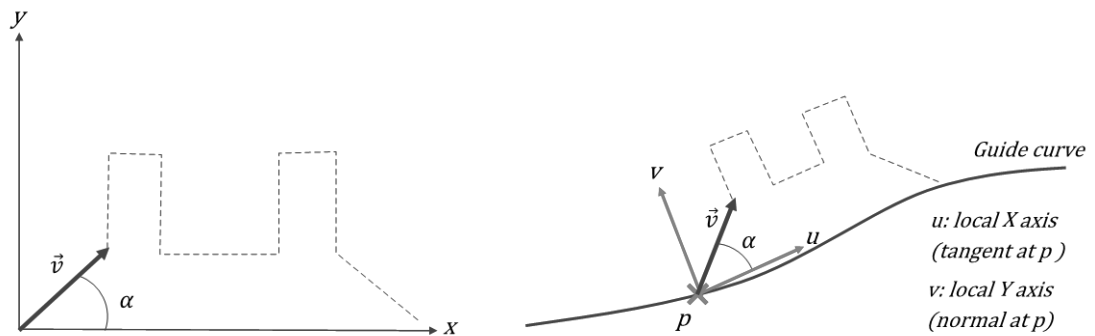
Figure 17: Reorienting vector sequence from global coordinate system (left) to local coordinate system at guide curve (right). $\vec{v}$: vector of vector sequence, α : reference angle, p : reference point,

The reference curve for the reorientation process is always the centerline of the current layer. The vectors of all the cells in the depth (thickness) direction of the wall are thus oriented based on the same reference points on the guide curve. This guarantees that all the cells fit neatly into each other. Figure 18 shows an exemplary print path layer of a corrugated wall element with internal cell structure. The dashed lines show the cell divisions in y direction (longitudinal to the wall) and show how the cells are mapped according to the corrugated guide curves and grid of divisions.
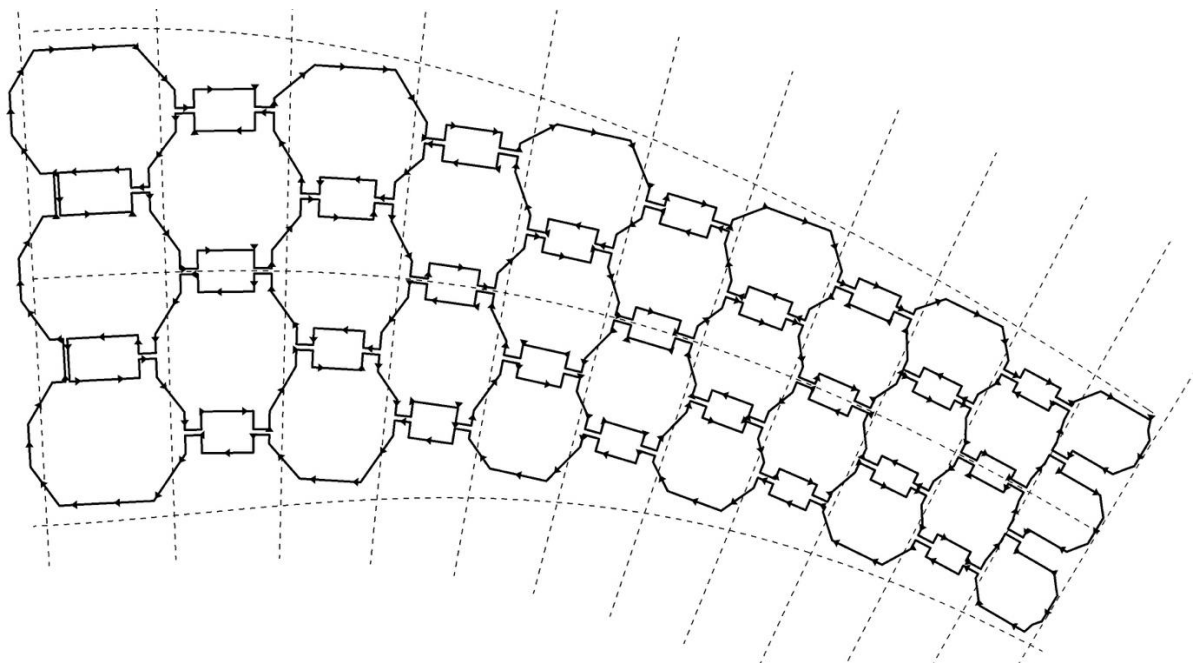
Figure 18: Exemplary print path layer of a corrugated wall element with internal cell structure

3.5. Variable cell sizes

A graduation of the internal cell structure can add multifunctionality to the 3D printed wall element. The cells can react to specific requirements such as wall thickness, thermal conductivity, or load bearing ability.

As described in paragraph 3.4 above, the print paths in every layer are calculated based on two boundary curves and their centerline. Splitting the centerline into sub curves defines the size of the cells in the direction of the centerline (x).

Besides a manual adjustment, an attractor point may be introduced to control the density of the cells inside the wall. Attractor points are a common concept in parametric design tools such as Grasshopper (Grashopper Primer V3.3, 2015). The attractor point may represent special punctual loads or other user desired anomalies in the wall element.

Variated cell sizes are calculated based on initial cell divisions in a wall element. The size of these initial cell divisions can be adjusted based on an average cell size. The attractor point then defines how division points are moved closer to each other based on the distance between the point itself and the point to be moved. When the initial cell divisions are gradually changed in size, additional cells are added automatically to fill potential gaps in the cell structure. The following formula defines the densification factor $f_{attractor}$ based on the distance from the attractor point P_{attr} to the division point P_{div} and the maximum distance d_{max} between the attractor point and all the division points on the guide curve.

$$f_{attractor} = \left(\frac{P_{div} - P_{attr}}{d_{max}} \right)^2 \qquad (3.6)$$

The distance from the centerline to either of the boundary curves defines the cell size in y direction. Because the number of cells is fixed, the depth d_y of the cells can be calculated by dividing the distance from centerline to boundary line $d_{center-boundary}$ by the number n of cells in y direction.

$$d_y = \frac{d_{center-boundary}}{n} \qquad (3.7)$$

3.6. Print path interpolation

For simplicity reasons and due to the limited amount of points the robot controller of the KUKA KR 150 L110 can scope with, paths between control points are interpolated as linear lines. This approach keeps the number of points minimal but can lead to sharp corners in the print path which may cause irregularities in the printing process. These irregularities include too much or too little material deposition due to varying robot velocities.

Beyond the scope of this thesis and specific robot model applied here, various approaches can be adopted to interpolate the print path in between the control points calculated by the vector sequence described in paragraph 3.3. By filleting corners with a given filleting distance, a smoother path without sharp edges can be generated. As shown on the left in Figure 19 below, straight lines in areas without corners remain. This still leads to robot acceleration and deceleration in areas with varying curvature.

A curved print path can be generated by interpolating a spline curve between the control points. As shown on the right in Figure 19 below, former straight lines are interpolated as curves as well. Despite the ability to adjust the number of control points to the curvature of the curve, this approach however yields the print path with most control points.
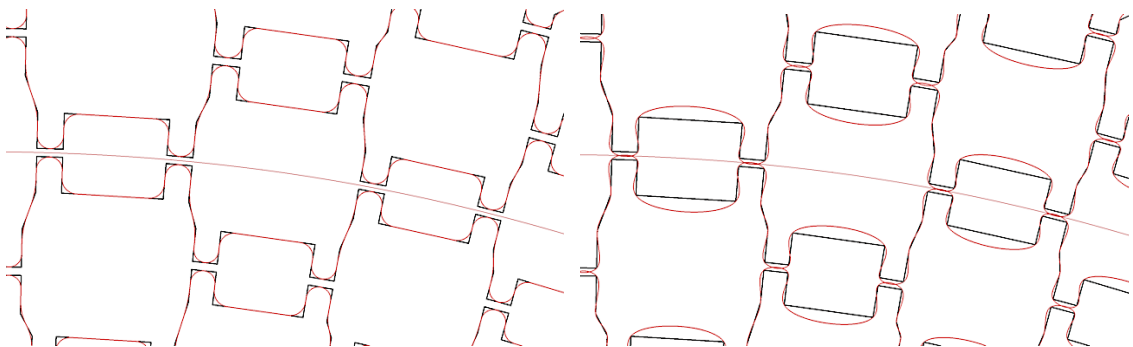
Figure 19: Linearly interpolated print path in black and filleted path in red (left). Linearly interpolated print path in black and cubic spline interpolated path in red (right).

The interpolated spline curve may aid in keeping the nozzle velocity constant and thus improve the uniformity of concrete deposition. It may however also produce vast amounts of data and lead to lower printing times. The robot controller model with its specific velocities and accelerations determines which interpolation method is best applied.

3.7. Correction factors for discrepancy between model and printed reality

Three distinct types of filament contacts can be identified. These include crossing paths, parallel running paths and paths which contact in just a single point. Figure 20 below shows the difference between the planned (black) and real print-path (dashed red). The initially high tensile strength of the printed filament leads to a filament displacement during the dynamic movement of the robot. Edges planned as sharp corners may thus turn out as round edges in the physical print. Henke et al. mention this discrepancy between planned and real geometry also in the context of gaps between parallel running filaments within the same layer. These gaps d can be caused by initial stiffening and shrinkage of the printed filaments (Henke, Talke and Winter, 2016, p.8).
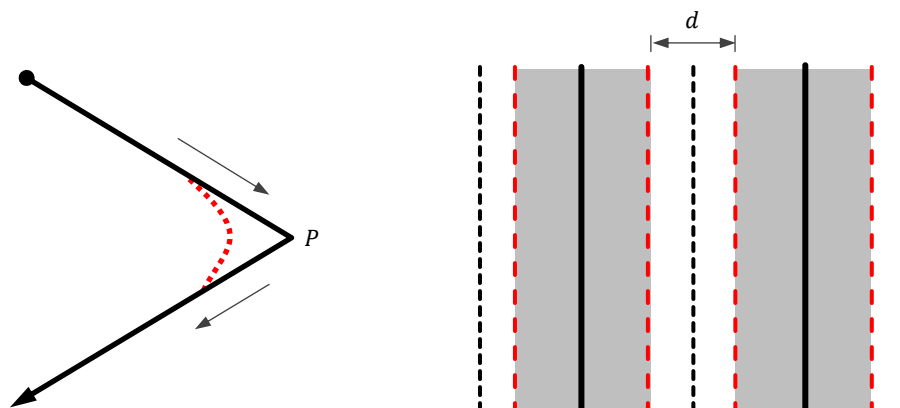
Figure 20: Scheme of planned print-path (black) compared to real print-path (dashed red). Behavior in corners (left) and parallel paths within the same layer (right) Adopted from: (Jin et al., 2014, p.4)

Additional user inputs are introduced in the design tool to compensate for the discrepancy and to ensure neighboring filaments are well bonded together. The correction factors include print path offset distances for parallel running and single point contacting paths. The correction factor d is derived from the expected shrinkage and robot movement observed in prior test prints.

3.8. Element joints

As explained in paragraph 2.3, layer cycle time significantly influences the concrete extrusion process. As the hydration of the concrete deteriorates layer to layer adhesion over time, layer cycle time is limited to a maximum length (Wangler et al., 2016, p.73). Therefore, the size of printed elements is limited – no matter whether the elements are prefabricated or printed in-situ. Printing large structures in multiple stages is thus necessary. The standard sizes of transportation vehicles additionally limit the size of off-site printed elements. Printing elements with geometrical joints can hence allow an easy and force-fit interconnection of multiple elements.

Within this thesis, joints are conceptualized to follow the logic of the internal cell structure. The cells themselves can thus create an interlocking connection between multiple elements. This is done by continuously printing the internal cell structure also on the outside of the element. The convex and concave areas of the cells form either female or male joints on each individual element. A high surface area in the joints is expected to be beneficial for a good transmission of forces and allow a tight connection of elements.

On at least one side of the element, printing the joint with two filaments next to each other is necessary to keep the start and end point of each layer identical. To make two joints fit, predicting the shrinkage and real print behavior of the concrete remains a challenge. In this work, the joints are thus designed with the tolerance of the print path width to compensate for the discrepancy of digital and real geometry. Figure 21 shows the print paths of a wall design composed of two elements joined together with cell like joints. Figure 22 shows a rendered top view of wall elements with cell like joint in between the elements. Figure 23 shows an axonometric rendering of two wall elements.

Element 1

Element joint *Element 2*
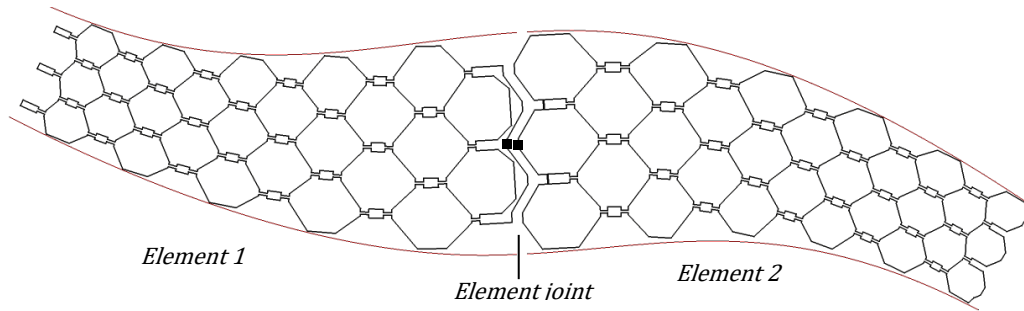
Figure 21: Print paths of a wall design composited of two elements joined together with cell like joints. Start and end of print paths marked with black dot.
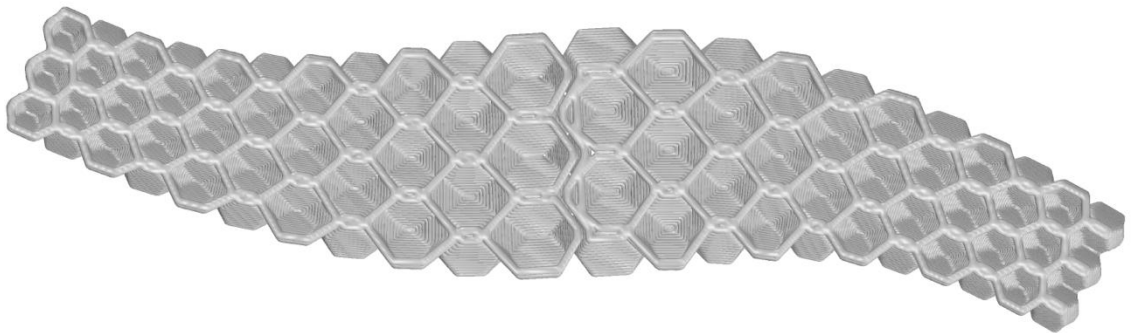
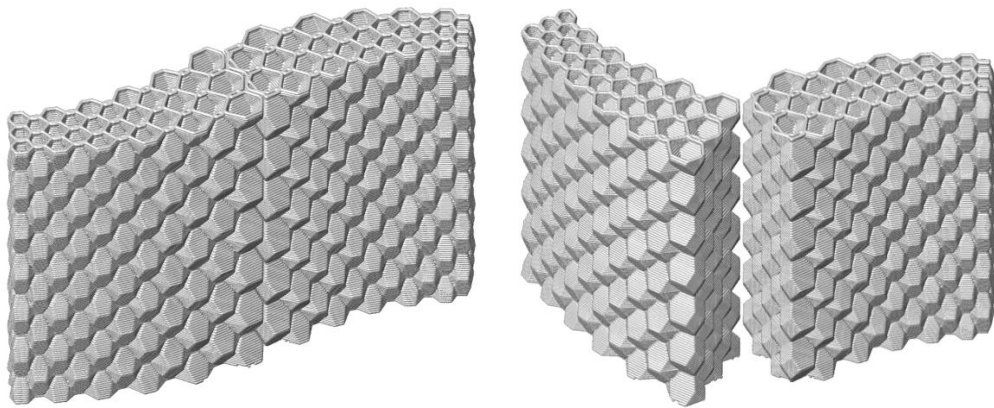**Figure 22: Top view of wall element rendering with cell like joint in between the elements**

Figure 23: Axonometric rendering of wall elements with cell like joint in between the elements

3.9. User feedback

3.9.1. Calculation of overhangs

As described in chapter 2.3.3 above, overhangs are a major constraint in extrusion based additive manufacturing. The buildability of the concrete mixture and the related layer cycle time define a maximum cantilever distance of the concrete filaments. To avoid printing failures, the design tool gives feedback about the expected overhangs during the design process.

As shown in the sections of cell structures in Figure 24, overhangs can be categorized in local and global overhangs. Local overhangs are caused only by overhanging parts of the undistorted closed cell geometry. The overhang of the whole 3D shape, meaning the combined overhang of several distorted cells, induces additional filament cantilevering called global overhang.
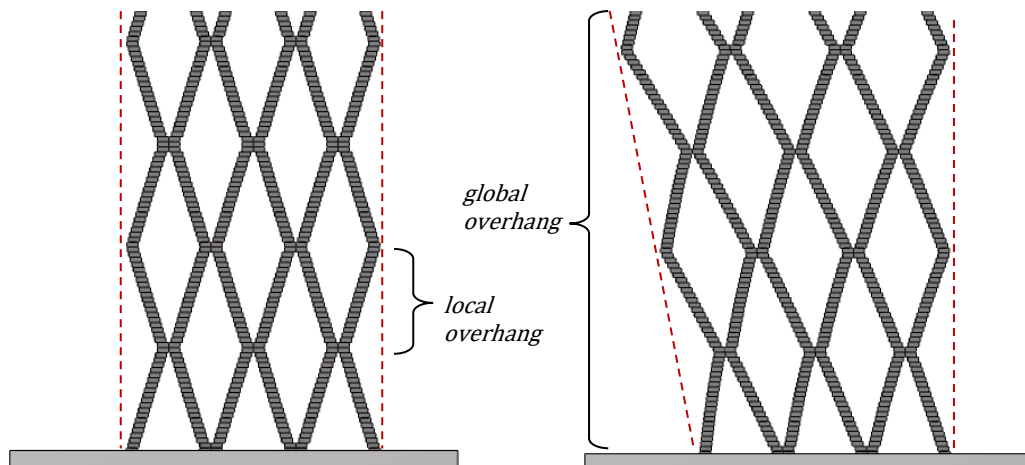
Figure 24: Section of cell structure with local overhang of undistorted cell geometry only (left) and section of cell structure with additional global overhang of distorted cells (right)

The overhang of a structure is defined by the distance a filament cantilevers over an underlying filament. The distance of cantilevering can thus be calculated as the projected horizontal spacing of consecutive print paths. To calculate the overhangs, the print path is split into segments at its corner points. As shown in Figure 25, the projected distance is then calculated from the midpoint P_1 of every segment, to the closest point P_2 on the underlying print path. The z-coordinates of the reference points P_1 and P_2 are set identical to calculate the distance projected into a horizontal plane.
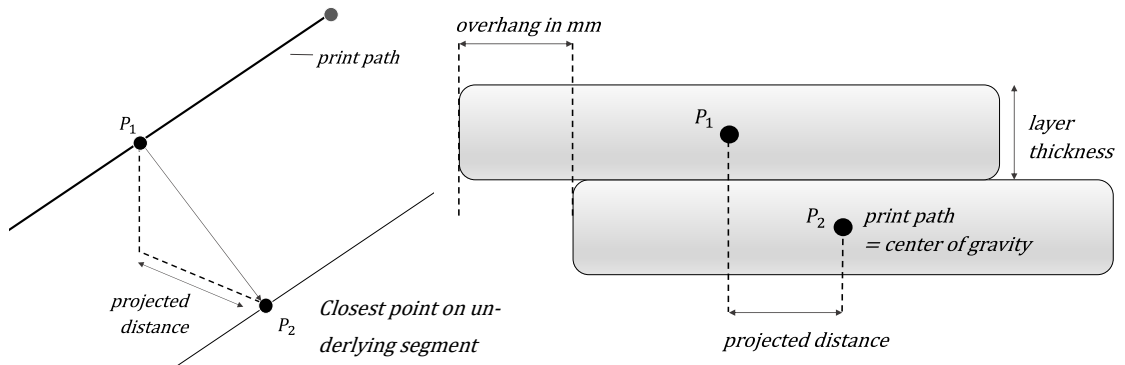
Figure 25: Reference points for overhang calculation (left) and projected distance calculation of filaments (right)

Very small segments of the print path are expected to be less critical despite having large overhangs. A segment length threshold is thus introduced in the overhang calculation to ignore overhangs if they occur only in very small areas in the print path. A feasible threshold is assumed to be the width of the printed filaments.

Inside the Rhino and Grasshopper environment, a false color rendering visualizes the calculated overhangs inside the modelled geometry. Figure 26 (left) below shows such a rendering exemplarily for the global overhangs in a multi corrugated wall element. Yellow and red highlight critical overhangs. Global overhangs are calculated based on the same method as the local overhangs, but with the geometry's boundary curves as reference. Figure 26 (right) shows an exemplary overhang analysis of a print path slice with possibly critical segments highlighted in red color.
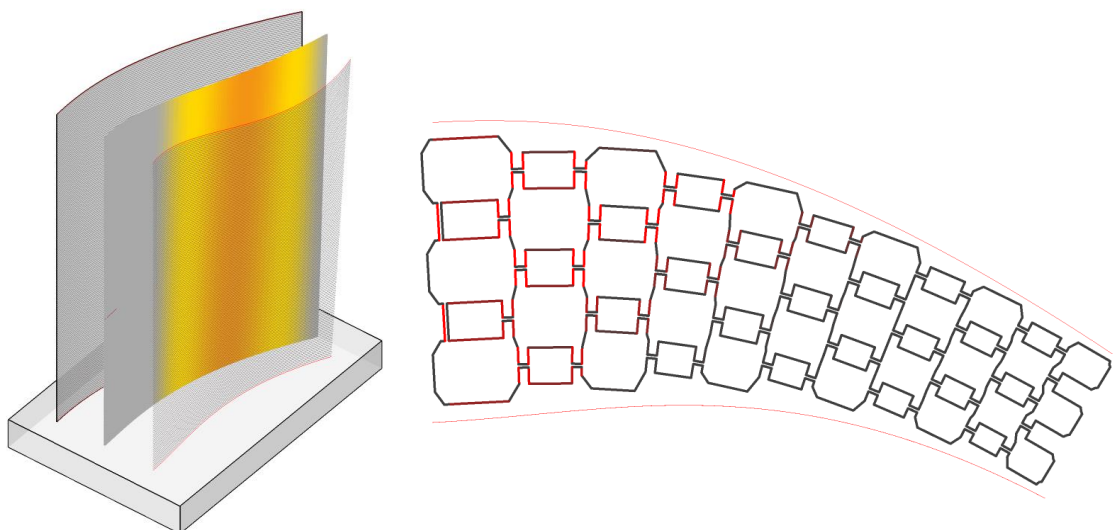
Figure 26: Visualization of global overhangs in digital model (left). Areas with critically high overhangs highlighted in yellow and red color.

3.9.2. Estimation of print duration

Layer cycle time significantly influences buildability as well as adhesion of consecutive layers (see paragraph 2.3). To guarantee a high-quality print, layer cycle time must be kept in certain boundaries defined by the concrete characteristics. The following print duration calculation can estimate the expected print time before printing.

The expected print duration is calculated based on the total length of the print path. As the robot has to decelerate and accelerate in corners, the robot speed can however not be assumed to be constant (Jin et al., 2014, p.4). A correction factor is thus applied to the print time calculated from the path length.

The correction factor f $[s]$ is based on the sum of angles α $[°]$ of changes in direction in the print path. The print path is split into segments at every corner point p. The angle α is then calculated between the adjacent tangent vectors $\vec{t}_1$ and $\vec{t}_2$.
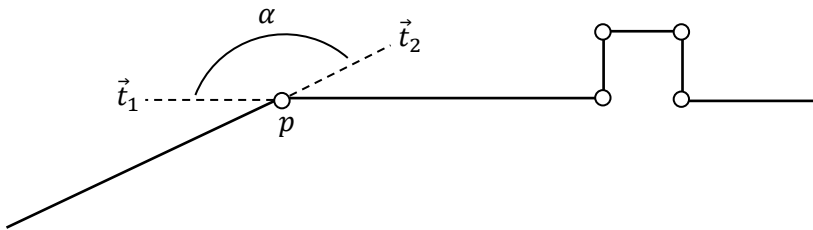
Introducing a calibration factor f_{robot} $[s/°]$ calibrates the correction factor to the specific robot model KUKA KR 150 L110.

$$f = \sum \alpha \cdot f_{robot} \tag{3.8}$$

The print time t_{layer} $[s]$ per layer with length l $[mm]$ and robot speed v_{robot} $[mm/s]$ is then calculated as:

$$t_{layer} = \frac{l}{v_{robot}} + f \tag{3.9}$$

Similar to the visualization of the overhangs, Figure 27 (left) shows how layer cycle times can also be visualized as false color overlay of an exemplary geometry design as well as on layer to layer basis in Figure 27 (right).
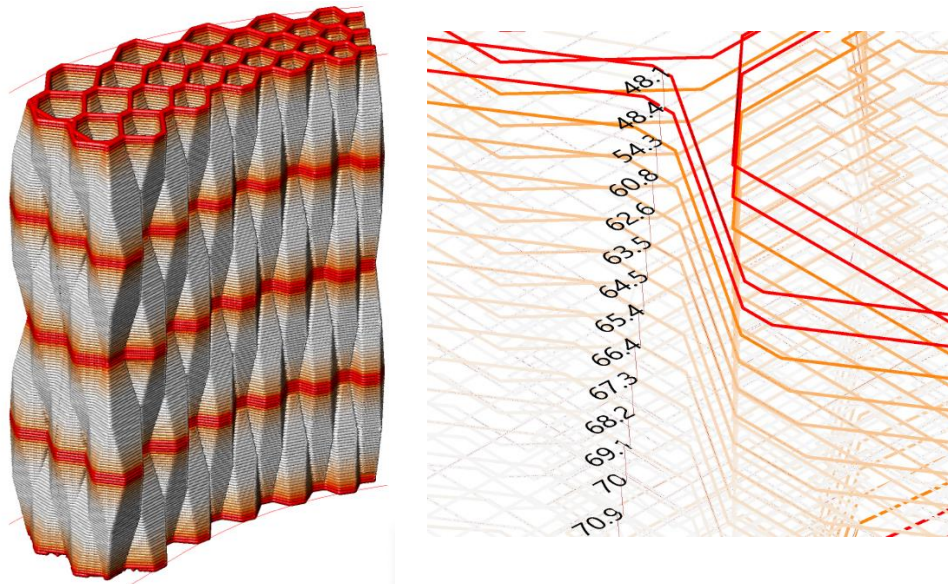
Figure 27: Visualization of layer cycle times in digital model (left). Layers with possibly too low and critically low cycle times highlighted in orange and red color. Visualization of print paths with indicated layer cycle times in seconds (right).

Within this thesis, the calibration factor $f_{robot}\ [s/°]$ is determined by measuring layer cycle times based on video recordings taken from prior test prints with comparable geometries.

3.9.3. Estimation of concrete volume and mass

Two approaches can be adopted to estimate the concrete volume and mass before printing: Either based on the printing time and feed rate of the concrete pump or based on the geometry and total length of the filaments and their density. Since the printing time and pump feed change dynamically depending on the machinery being involved, the geometry-based approach is adopted within this thesis. The expected concrete volume $V[m^3]$ is given as:

$$V = l \cdot \frac{b \cdot h}{10^6} \tag{3.10}$$

Where $l[m]$ is the total length of the print path, $b[mm]$ the width of the concrete filament and $h[mm]$ the layer height. The concrete mass $m[kg]$ can then be calculated based on the density $\rho_{concrete}[kg/m^3]$ as:

$$m = V \cdot \rho_{concrete} \tag{3.11}$$

3.9.4. Estimation of heat transfer

Two different approaches are adopted to estimate the thermal performance of a designed building element. The first approach is based on a thermal bridging simulation performed on the explicit horizontal cross-section of the geometry. The second approach is based on a simplified representation of the geometry and is based on the calculation of heat transfer coefficients.

The thermal bridge software LBNL THERM 7.4 is used to estimate the thermal insulation performance during the design process (Lawrence Berkeley National Laboratory and National Fenestration Rating Council, 2015). The simulation software can be implemented in the design process through the Grasshopper plugin Ladybug (Sadeghipour Roudsari and Pak, 2013). The calculation code is well verified in accordance to BS EN ISO 10077-2, which is the reference measure for heat transfer calculations (Nammi et al., 2014).

The calculation of THERM is based on a two-dimensional simulation model. The three types of heat transfer are modelled as follows: Conduction and radiation are both modelled explicitly via Finite-Element-Method (FEM) and view-factor calculation. Convection is estimated via correlations and heat transfer coefficients derived from rectangular air-filled cavities (Huizenga et al., 1999, p.1). This method is not exact in calculating the convection in closed cells but precise enough for an early estimation. Consequently, the estimated calculations of the THERM simulation are expected to give simplified and fast feedback to the user.

To generate the simulation geometry, the calculated print path of a single layer is offset to create boundary curves which represent the concrete filaments. The offset algorithm 'Clipper' is used to create the offset curves from the print path (Johnson, 2010) with the required precision for the THERM simulation. The resulting closed polygons represent the cells and distinguish air filled regions from concrete filled regions.

The outer boundary curves of the layer are linked to their corresponding boundary conditions. The boundary curves, which mark the connection between neighboring elements, are set to be adiabatic. This means that the temperatures on both sides of the boundary are assumed to be identical. The remaining boundaries are set to represent indoor and outdoor conditions. The indoor condition is set to 20°C, the outdoor condition to -5°C. These conditions are just the standard testing conditions and have a neglectable

influence on the simulation result (Nammi et al., 2014). The film coefficient is set to 7,7 W/m²K for the indoor boundary and to 25 W/m²K for the outdoor boundary (DIN EN ISO 6946, 2018). The simulation mesh is generated inside the THERM simulation engine. THERMs highest mesh level of degree eight is used to obtain a mesh representation of the geometry. Figure 28 shows an exemplary layer of a wall element with the simulation mesh and its corresponding boundary settings. Grey color shows concrete filled areas and white color air filled cavities.
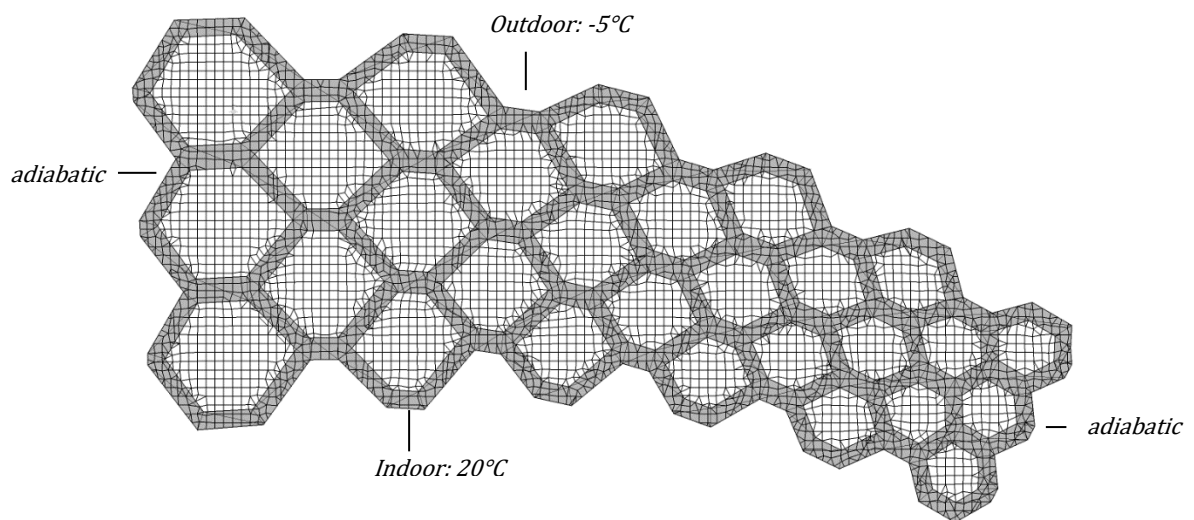
Figure 28: Visualization of THERM simulation mesh and its boundary conditions.

The simulation of the explicit geometry is complemented by simulations of simplified represenatives of the geometry for two reasons: Firstly, the complexity of the explicit geometry is expected to cause unexpected irregularites in the mesh which may disturb the validity of the results and cause very long calculation times. Secondly, the simulation performed on the freeform geometry is not appropriate to asses the U-Value of the cell structure in a specific cross-section location. This is due to the fact that both wall thickness and cell sizes vary throughout the geometry.

The simplified cell geometry represenation is created based on the number and size of cells, width of concrete filaments and total thickness of the wall in specific cross-section location. These parameters can be adjusted parametically to create the simplified model along with explicit geometry. Cells in the simplified model are created as simple rectangles.

To verify the simulation against the code of building standards, the simplified geometry is calculated with standard heat transfer coeefficient calculations as well. As described in paragraph 2.2.2, the heat transfer coefficient of a building element is defined in DIN EN ISO 6946 as the U-Value [W/m²K]. It is calculated as the reciprocal of a sum of heat transfer resistances. This method is adopted to estimate the heat transfer in the cell structure developed within the scope of this thesis. The aggregated heat transfer coefficient R_{cell} of any cell in the direction of heat transfer can thus be defined as:

$$R_{cell} = \frac{A_{cavity} \cdot R_{cavity} + A_{concrete} \cdot \frac{d_{concrete}}{\lambda_{concrete}}}{A_{cavity} + A_{concrete}}$$

(3.12)

The thickness of the concrete boundaries $d_{concrete}[m]$ euqals the filament width. The amount of the respective materials is calculated based on their cross-section areas A_{cavity} and $A_{concrete}[m^2]$. $\lambda_{concrete}$ is the thermal conductivity of the concrete. The heat transfer resistances of the air cavities $R_{cavity}[\text{m}^2\text{K/W}]$ are taken as table values from Table 2 in paragraph 2.2.2. The heat transfer resistance for airflow on the inside and outside surface of the wall element are given as R$_{si}$ = 0,13 m²·K/W and R$_{se}$ 0,04 m²·K/W (DIN EN ISO 6946, Table 7). The U-Value $U_{wall}[W/m^2\text{K}]$ of the wall cross-section is then calculated as:

$$U_{wall} = \frac{1}{R_{si} + \sum R_{cell} + R_{se}}$$

(3.13)

For the specific case of this thesis, the density and thermal conductivity of the lightweight concrete are assumed according to the assessment of Henke, Talke and Winter as follows: The density is assumed to be 1.300 kg/m³ and its thermal conductivity is given with 0,33 W/m*K (Henke, Talke and Winter, 2017).

4. Lightweight concrete 3D printing process

4.1. Process

Figure 29: Robotic setup of printing process at Technical University of Munich

A standard industrial 6-axis robot places the filaments according to the planned print paths. The model used at Technical University of Munich is a KUKA KR 150 L110 with a reach of 3.5 m. As shown in Figure 29 above, the robot is fixed to a 7th linear axis to enlarge the possible working area.

As the controller of the robot does not allow any live communication between design environment and robot, the print paths must be translated to machine instructions (G-Code) before being sent to the robot controller. The software KUKA-PRC is applied for this translation process. KUKA-PRC integrates as a plugin in the Rhino and Grasshopper environment (McNeel & Associates, 2019). The software can also simulate the printing process to identify conflicts or unreachable coordinates.

The concrete is premixed in small batches and then pumped through a 25 mm wide and 10 m long hose. The hose is connected to an end-effector with a printing nozzle. A Knauf PFT Swing L FC-400V concrete pump conveys the concrete from the mixer to the nozzle. On average, the pump works with a federate of 3.0 kg/min. To avoid overheating of the material, the conveyer-screw of the pump is cooled under running water constantly.

The end effector is a custom-made rig with a hose connection and nozzle bracket. A quick-change system on the nozzle bracket allows easy interchanging of nozzles (Henke et al., 2018). Control points of a polyline print path define the robot end effector positions. Every control point is translated to a plane which defines the end effector position and orientation. The robot controller interpolates the robot movement as linear lines between control points.

The demonstrator objects in this thesis are printed with a round nozzle of 22 mm diameter. Unlike rectangular nozzles, round nozzles cause clearly visible filaments in the finished elements but can be used without having to orientate the nozzle tangential to the print path. Not having to orientate the end effector with the 6th axis of the robot makes the process more robust and can also increase the printing speed (Henke et al., 2018, pp.20–24).

Spraying the elements with water and wrapping them in foil after printing keeps the elements moist. This process avoids cracks caused by drying of the concrete. Compared to massive concrete, the printed elements dry relatively fast due to their high surface area and lack of formwork which could protect against air exposure (Ngo et al., 2018, p.181).

4.2. Material

Characteristic about the 3D printing process described here is the material used. The 3D printing process, which is developed at Technical University of Munich, applies lightweight concrete as extrusion material. The lightweight concrete consists of cement, water and lightweight aggregates.

The concrete mixture used for printing the demonstrator objects designed within the scope of this thesis contains expanded glass granulate as lightweight aggregate. As reported by the manufacturer *Poraver*, the expanded glass is made exclusively from recycled waste glass (Dennert Poraver GmbH, 2020).

Despite its low density of 300 – 900 kg/m^3, the porous granulate has a relatively high resistance to pressure of 1,4 – 1,8 N/mm^2 (Matthäus et al., 2020). Ordinary Portland Cement and Portland Limestone Cement are used as cementous binders (Matthäus et al., 2020).

By replacing rocks and sand with lightweight aggregates, not only the density, but also the thermal conductivity of the concrete is reduced accordingly. Air being trapped in the pores of the porous aggregates is the reason for the reduced thermal conductivity. Conventional concrete, at a density of 2000 kg/m^3, has a thermal conductivity of about 1,6 W/m*K (DIN 4108-4, 2017). The lightweight concrete presented here has a thermal conductivity of 0,33 W/m*K and a density of 1300 kg/m^3 (Matthäus et al., 2020).

5. Results - Printing of a demonstrator object

To validate the feasibility of the developed structure and design tool, the design tool described in chapter 3 is applied to design wall like demonstrator objects. Two demonstrator objects are then printed at the Robotic Fabrication Lab at the Technical University of Munich. Chapter 4 describes the related process, robotics and material characterization. The following chapter is structured in a description of the application of the design tool followed by a description of the outcome of the demonstrator printing.

5.1. Wall element design

Throughout the following paragraphs, the two demonstrators are referred to as demonstrator 'A' and 'B'. Table 4 below shows a summary of the main characteristics of the designed demonstrator objects.

Table 4: Summary of characteristics of demonstrator objects in design phase

	Demonstrator 'A'	Demonstrator 'B'
Base dimensions	120 x 80 cm	120 x 80 cm
Element height	1,04 m	1,04 m
Layers	116 layers à 9 mm	116 layers à 9 mm
Cell height	74 cm	24,4 cm
Maximum overhang per layer	4,1 mm	6,2 mm
Thickness	24 – 45 cm	24 – 45 cm
Cell diameter	34 – 87 mm	34 – 87 mm
Total print path length	1666,4 m	1666,2 m
Estimated weight	427 kg	427 kg

Both demonstrator objects are designed to fit on a single pallet with the dimensions of 120 x 80 cm to allow easy transportation. The dimensions of the demonstrators are 1.0 m length, 0.45 to 0.25 m width and 1.04 m height. The shape of the wall is defined by two corrugated surfaces leading to a freeform element with one wide and one narrow end. The sizes of the cells are adjusted to change their sizes gradually from small to large. The start and end joints are designed to allow the connection of additional elements. An outer shell of the wall is left out intentionally to show the internal cell structure also to the outside. All the parameters can be adjusted parametrically within the developed design tool. Figure 30 below shows the guide surfaces which define the shape of the wall design (left) the calculated continuous print paths (middle) and a rendering of the demonstrator 'A' wall elements with graded cell sizes (right).
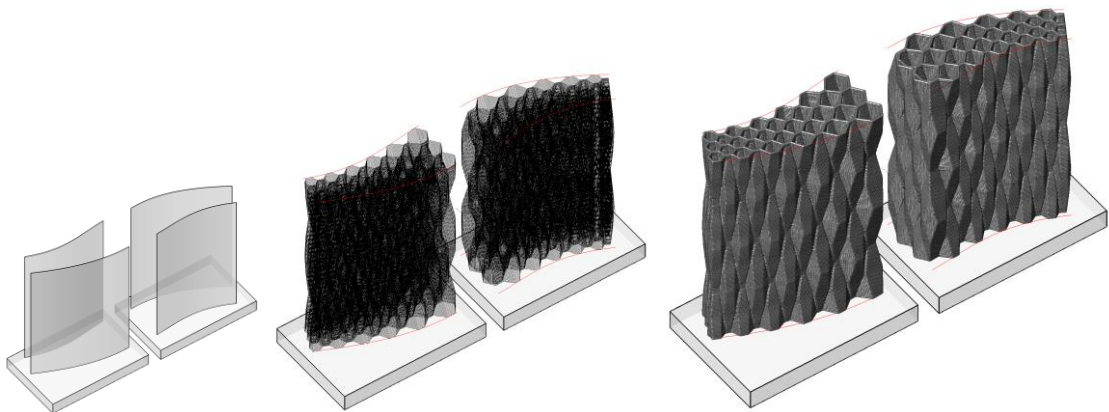
Figure 30: Rendering of guide surfaces (left), rendering of print path of demonstrator object (middle) and rendering of printed geometry (right)

The height of the cells in demonstrator 'A' is set to 0.74 m, which is defined by a desired maximum overhang of 4 mm and an average cell width of 60 mm. To assess the stability of the cell structure, a second element is printed with an increased maximum overhang of 6.2 mm and a cell height of 0.37 m.

Figure 31 below shows the overhang visualization of layer 68 in demonstrator 'A' on the left and demonstrator 'B' on the right. The greatest overhangs can generally be observed in the greatest cells. The reduced height of the cells in demonstrator B also leads to higher overhangs.
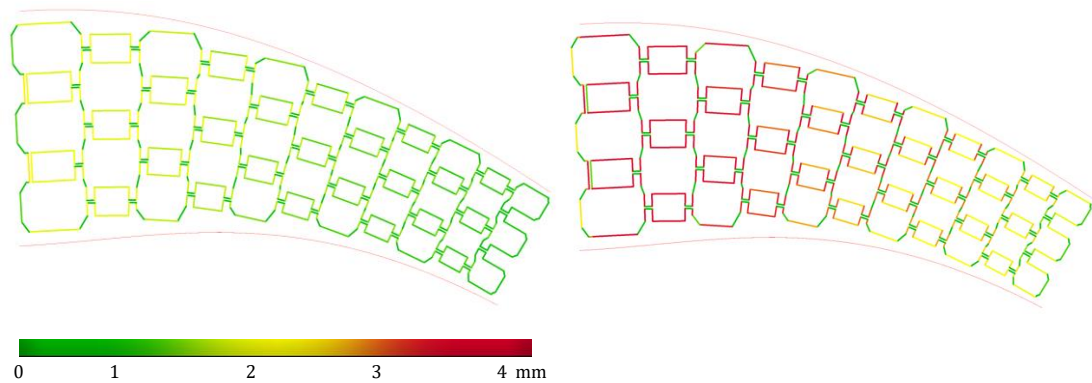
Figure 31: Visualization of overhangs in digital print path model of layer 68 in demonstrator A (left) and B (right). Areas with critical overhangs highlighted in red color.

Based on the material mix described in 4.2, an ideal layer cycle time of roughly one minute is predetermined. At an average robot speed of 120 mm/s, a minimum path length of 7.0 m per layer is preset. The path length is calculated to be in between 7.8 m and 13.0 m for the first and between 7.8 m and 12.9 m for the second element. The calculated total path length and estimated weight are identical in each of the elements.

At a layer height of 9 mm, the designed wall elements are split into a total number of 116 layers each. For stability reasons, the first layer is set to print maximal open cells on the outermost cell row. The same layer is also chosen as the top layer of the element. No filaments are added on the outermost cell rows to show the internal cell structure of the wall element also to the outside.

5.2. Printability

Figure 32 below shows the finished demonstrator objects. Demonstrator 'A' on the left and demonstrator 'B' on the right. As described in the latter paragraph 5.1, demonstrator 'A' and 'B' were designed identical apart from the cell height and related overhangs.
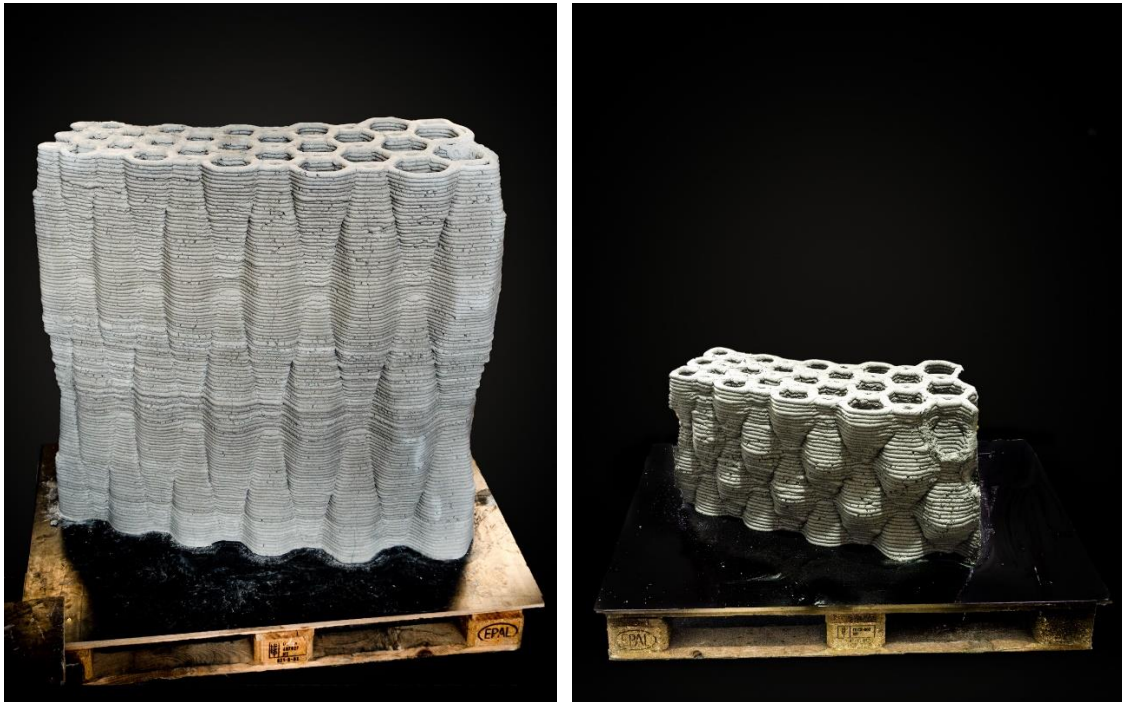
Figure 32: 3D printed demonstrator object 'A' with cell height of 74 cm (left) and demonstrator 'B' with smaller cells (right)

For demonstrator A, the cell structure proved to be stable during the printing process. No collapsing could be observed during the printing process. The maximum overhang in the printed structure is 3,3 mm. At a layer thickness of 9 mm, this equals a deviation from verticality of 20°. A total number of 116 layers could be printed without interruptions.

Demonstrator 'B' with a cell height of only 37 cm proved the feasibility of overhangs of up to 6,2 mm for neighbor supported cells. At a layer thickness of 9 mm this equals an overhang angle of 35°. Printing of most overhangs rated non-critical in the preprint check was without issues. An exception are the outermost cells in demonstrator 'B' with larger overhangs. As shown in Figure 33, the outermost cells collapsed during the printing process. Due to the collapsing cells, printing of this demonstrator was aborted after 46 layers.
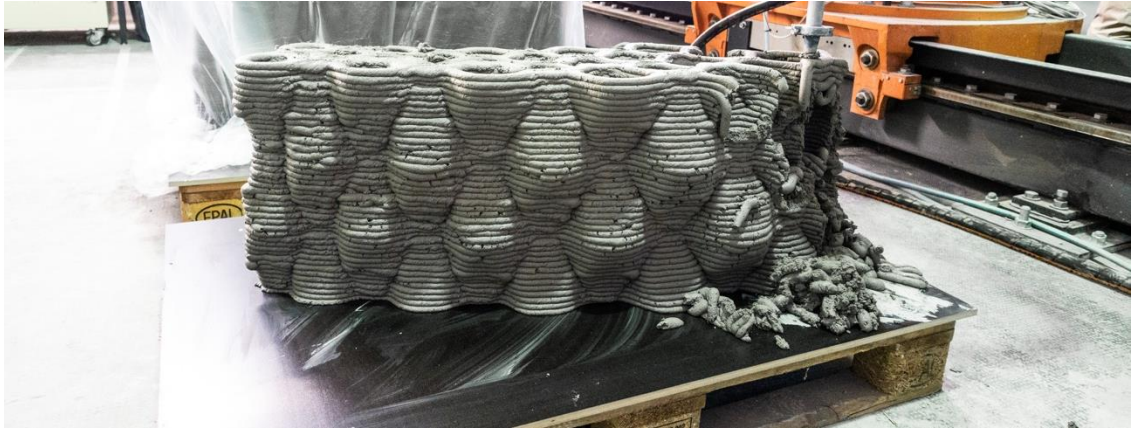
Figure 33: Collapsing of outermost cells in demonstrator object with cell height of 24 cm

In consequence of the continuous print path planning, both demonstrators were printed without the necessity of interruptions in material deposition and concrete pumping. Printing of the large demonstrator 'A' took 3,5 hours to completion.

5.3. Discrepancy between digital model and printed reality

The printed results show that the compensation factors for parallel running and touching print paths can counteract the discrepancy between digital and real geometry. Figure 34 below shows an image of a print path layer printed without the correction factor on the left and a layer printed with the correction factors on the right. A small gap between the filaments can be observed on the left, whereas well bonded parallel running and touching print paths can be observed on the right. A distance of 5 mm between print paths for filaments of roughly 22 mm width shows to be appropriate for the specific printing setup used in this thesis.

Figure 34: Weakly bonded parallel filaments with small gap in between the filaments (left) and well bonded partly overlapping filaments (right)

During printing, the real layer cycle times of several layers were measured. Table 5 below shows the measured and predicted cycle times of several layers. With a correction factor $f_{robot} = 0{,}033\ [s/°]$ an average deviation of 1,3 % between predicted and real layer cycle time can be calculated.

Table 5: Comparison of predicted and measured layer cycle times

Layer	Predicted cycle time	Measured cycle time	Deviation
5	59,9 seconds	62 seconds	3,4 %
35	65,5 seconds	64 seconds	2,3 %
50	69,1 seconds	70 seconds	1,3 %
7-81	Ø 70,4 seconds	Ø 71,3 seconds	Ø 1,3 %

5.4. Heat transfer in wall elements with internal air cavities

Based on the method described in paragraph 3.9.4, the heat transfer coefficient of the printed element is estimated for individual two-dimensional layers of the element. Figure 35 below shows the visualization of the THERM simulation results for layer 32 and 68 of demonstrator 'A' as examples. Figure 28 (left) shows layer 32. Figure 28 (right) shows layer 68. A false-color rendering of the heat flux results is shown in Figure 28 (upper part), the corresponding meshing in the middle and layer cross-section in the lower part. Shades of blue show lower heat flux below 15 W/m², shades of green show medium heat flux and shades of red and orange show high heat flux above 30 W/m².

In the heat flux graphic, a tendency of lower heat flux inside the cells than in the concrete around the cells can be observed. This is less applicable for the largest cells of both layers. The heat flux in the air cavities ranges from 10 W/m2 in the smallest cells and up to 20 W/m² in the largest cell cross-sections. The narrow end of the geometry shows higher heat flux in the concrete in red and orange. Low heat flux below 15 W/m² can be seen on the outermost edges of the layers in blue colors. The density of the mesh created by THERM is not homogeneous throughout the layer as it shows extremely small elements in some areas.
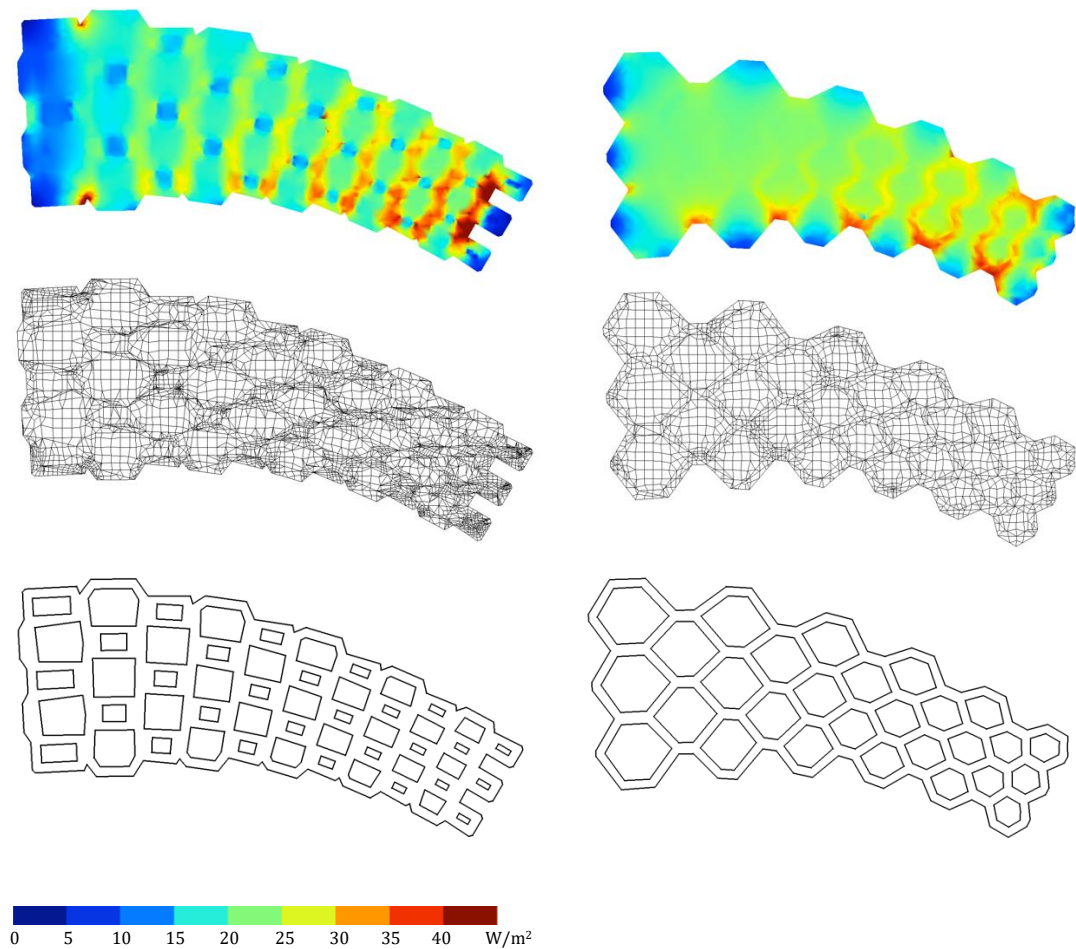
Figure 35: Visualization of heat flux (upper part) simulation mesh (middle) and layer geometry (lower part) as horizontal section of cell structure in layer 32 (left) and layer 68 (right). Heat flux calculated with LBNL THERM 7.6

As mentioned in paragraph 3.9.4 earlier in this thesis, the simulation performed on the freeform geometry is not appropriate to asses the U-Value of the cell structure in a specific cross-section location. This is due to the fact that both wall thickness and cell sizes vary throughout the geometry. U-Value calculations are thus performed on simplified represenations of the geometry.

To assess the effectiveness of air cavities inside a lightweight concrete wall element, an element with cavities is compared to a massive element with identical thermal properties. This procedure is also applied to evaluate the results of the thermal heat transfer simulation. A wall panel with a desired U-Value of 0,5 W/m²K is taken as reference for this comparison. Based on the DIN EN ISO 6946, a wall with a total thickness of 0,5 m, equipped with eight layers of air cavities of 40 mm in width and depth was calculated to achieve the desired U-Value of 0,5 W/m²K. Figure 36 (left) shows a graphical represenation of the simplified cell model. Figure 36 (right) shows the results

of the heat flux calculation in the simplified structure. THERM calculated the U-Value of the structure to be 0,48 W/m²K. This is a deviation of 4% compared to the U-Value calculated based on DIN EN ISO 6949.
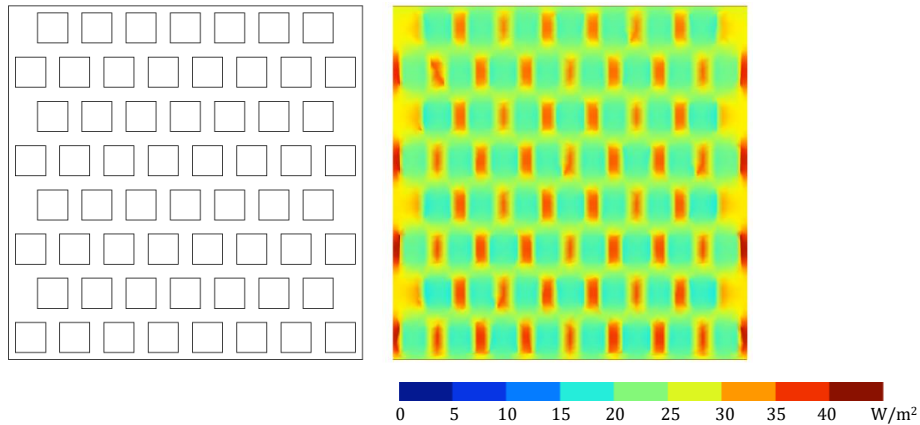
Figure 36: Drawing of simplified cell structure model (left) and false color rendering of the heat flux in the structure (right). Heat flux calculated with LBNL THERM 7.6

Table 6 below shows that the element with cavities achieves the same performance as the massive element but with 8,5 cm less thickness. This equals a reduction in thickness of 15%. Due to the lower densitiy of the element with cavities, 51% of the concrete mass can be saved while achieving the same thermal performance.

Table 6: Comparison of massive wall and wall with air cavities based on DIN EN ISO 6949 U-Value calculations

	Massive wall	Wall with internal cell structure
U - Value	0,5 W/m²K	0,5 W/m²K
Thickness	58,5 cm	50,0 cm
Mass	760 kg/m²	369 kg/m²

6. Conclusion

6.1. Discussion

In this thesis, a concept of printing cellular structures inside a freeform wall element produced by additive manufacturing with lightweight concrete could be demonstrated. In the following paragraphs, the concept and results of its application are discussed against feasibility, sustainability and other literature.

6.1.1. Overhangs and print resolution

It could be demonstrated within this thesis, that 3D lightweight concrete printing can be applied to print building elements with internal cellular structures. In particular, the achievable overhangs proved to be sufficient to print closed cells. Even though, in terms of achievable cell sizes and design freedom, limitations are still present.

As reported in paragraph 5.2, the outermost cells of demonstrator 'B' collapsed during the printing process. This suggests that neighboring cells structurally support each other and thus allow steeper overhangs than non-supported cells. This hypothesis is supported by Bos et al. who identified the filament mass placed in the plane of cantilevering as an influencing factor for the ability to produce overhangs (2016, p.219).

Bekkouche et al. argue that cell sizes of 40 – 60 mm (Bekkouche et al., 2013) are ideal in terms of heat flux reduction. With filament widths ranging around 20 mm, printing such small cells is fundamentally possible but comes with the drawback of a relatively high concrete density in areas of small cells. As seen in Figure 35 and Figure 36, the concrete boundaries of the cells act as thermal bridges and conduct much more energy than the cavities. The proportion of cell volume to concrete boundary has thus a major influence on the thermal performance of the cell structure. Improving this proportion is currently limited by the comparably low print resolution of the applied printing process. With the current printing process, it is hence not possible to achieve sufficient resolution to print such small cells with respectively low concrete boundary widths. Since smaller filament widths slow down the built rate, print resolution cannot be reduced without the drawback of long print times. Faster printing processes might overcome this issue in the future, until then, desired print resolution and acceptable print time need to be balanced according to individual needs.

6.1.2. Design tool and print path planning

Regarding the modelling of the print path, Gosselin et al. argue that conventional slicing operations are not well suited for construction scale printing applications and special tools need to be developed for this use-case (2016, p.103). Jin et al. report about an optimization method they use to link several sliced print paths to a single continuous path with the aim to avoid printing interruptions and time loss caused by air travel of the end effector. In their conclusion they remark that their algorithm could need further optimisation in the case of complex geometries (2014, p.32).

In this respect, the work of this thesis provides a possible enhancement by implementing print path continuity inherent in the design system. Successful printing of two wall elements with internal cellular structures could demonstrate that even complex geometries may be printed in a continuous print path. The applied "bottom-up" method of a sequence of parametrically adjusted vectors seems to be appropriate to define the desired continuous print paths and could provide an alternative to classical slicing operations. Assuming the emergence of new printing processes, in which printing interruptions are not an issue, the necessity of path continuity may become obsolete in the future. Despite this, continuous prints will likely remain advantageous due to time loss caused by non-printing air travel and in non-continuous print paths (Jin et al., 2014, p.2).

Buswell et al. argue that a wide distribution of 3D concrete printing technology is being hampered by the lack of 3D printing experts with necessary expertise to use complex design and machinery (2018, p.37). The development in this thesis tries to counteract this problem by providing an easy to use design tool that guides the user to a printable design. The pre-print calculations provided in this work are based on rather simple assumptions but in turn also provide fast and direct feedback allowing an iterative refinement of the design.

Instead of refining geometry in an iterative feedback-based approach, optimization algorithms can be applied to refine a geometry as well. Kontovourkis, Tryfonos and Georgiou use a topology optimization algorithm to structurally optimize a 3D clay printed wall element (2019). Bhooshan et al. transfer an equilibrium-based modelling approach usually used for the calculation of brick walls to calculate the time dependant contact forces between 3D printed filaments. These examples demonstrate the possibility to implement even complex pre-print simulations to estimate the printability and performance of complex structures. While these simulations ensure a high conformity of digital and physical

model, more input data and computational effort is necessary as well. By considering the dynamics of the rheological and structural behaviour of the concrete filaments, issues such as the collapsing of the outermost cells during the printing of demonstrator 'B' could possibly have been predicted before the printing.

6.1.3. Performance feedback

The design tool developed within this thesis features a feedback system which estimates the thermal performance of a designed structure during the design process. Based on simulations and calculations of heat transfer coefficients, a potential reduction of 15% in wall thickness and about 50% in wall mass could be estimated in a comparision of a massive element to an element with internal cell structure.

It has to be noted that the heat transfer calculation described in paragraph 3.9.4 is based on a two dimensional representation of the internal cell geometries. While conduction and radiation are modelled explicitly in a finite element model, convective heat transfer in the air cavities is only calculated by static heat transfer coefficients (Huizenga et al., 1999, p.1). The effect of the cell geometry on a possibly reduced convection in the cell can thus not be considered in the simulation. Limitations of the THERM simulation could also be identified regarding the complexity of the geometry. While the simulation runs succesfull for most simplified layer geometries, the Finite Element meshing shows irregularites in complex layers. These irregularities may lead to unexpected anomalies in the simulation results. As shown in Figure 35, these irregularities may be caused by inhomogeneous simulation meshes. When applied to complex layer geometries, the reliability of the applied simulation method may thus be questionable. At this stage of development, simplified geometry represenations and calculations based on heat transfer coeefficients seem to be more appropriate to give at least qualitative performance feedback.

All in all, it has to be clarified that the numbers statet above were calculated based on simplified assumtions and with the above mentioned limitations in the applied simulation method. Although the cell structure is likely enhancing the thermal performance of a 3D printed concrete element, this hypothesis still has to be prooven via measurements. The same is true for detecting the ideal ratio of cell size to concrete boundary dimensions. Their dimensions need to balance betweem thermal performance and load bearing capacity.

Eventhough, within this thesis, an enhanced thermal performance of the developed structure could not be proven by measurements, scarce reports of such measurements on other 3D concrete printed structures exist in literature. Prasittisopin et al. performed measurements on a 3D concrete printed guardhouse in the hot tropical climate of Thailand. The guardhouse was printed with a single layered woven structure with internal voids. Measurements of the indoor surface temperatures of both conventional and additively manufactured construction revealed a reduction of the surface temperatures by 12% in the additively manufactured construction (Prasittisopin et al., 2019, p.25). In addition, a beneficial self shading effect of the wooven surface could be observed. It is likely that a self shading and insulating effect also applies for the cell surface of the elements developed in this thesis.

6.1.4. Sustainability and Multifunctionality

In this thesis it could be shown that additional functionality can be added to a 3D printed wall element equipped with internal cellular structures. A simple design tool can be used to design a multifunctional wall element in conjunction with calculating machine paths for 3D printing. Multifunctionality can be added by integrating graded internal cell structures and allow freeform corrugated geometries at the same time.

Agustí-Juan and Habert support this hypothesis by arguing that the environmental and economic impact of the 3D printing process is relatively low in comparison to the material production. As the extra effort of the machinery in the printing process is almost neglectable, the potential to reduce material consumption by adding functionality in 3D printing is high. Nevertheless, they also remark that the benefit of the added functionality can only be fully exploited when the environmental impact of the equivalent function in a conventional construction is high. Otherwise the benefit of the added functionality might be neglectable (Agustí-Juan and Habert, 2017, p.19).

In a study of a self-shading brick wall, Agustí-Juan and Habert assess that a conventional wall with a thin layer of insulation has a better environmental performance than a digitally fabricated one. The digital fabricated wall could not prove to be beneficial in this case, because the additional function of self shading did not have a big impact in the conventional construction (Agustí-Juan and Habert, 2017, p.19). Transferred to this work, this means that the benefit of the additional function of thermally enhancing cell structures needs to be questioned in comparison to the conventional alternative. Cheap additional insulation is mostly applied as Exterior Insulation and Finish Systems (EIFS).

According to Albrecht and Schwitalla, these petrol based additional layers are hard to recycle and should therefore be avoided (Albrecht and Schwitalla, 2015, p.7). Mono material constructions, as presented in this thesis could provide an alternative. On the other hand, sustainable insulation can also be realized as multi layered construction when reusable and renewable materials are used (Albrecht and Schwitalla, 2015).

As argued by De Schutter et al., the greatest benefit of 3D concrete printing is the possibility to produce complex structures which could otherwise not be produced, or at least only with a great amount of effort (2018). Allowing highly customized architecture with a new design language of freeform design could thus enrich architecture also from a viewpoint of socio-economic sustainability.

Even though multifunctionality and optimized material placement can reduce the amount of material used, concrete production is still a highly energy consuming process (Lehne and Preston, 2018, p.6). Applying smaller impact materials based on renewable or recycled resources could supply an alternative to concrete. For example, Kontovourkis and Tryfonos developed a 3D printing process based on clay (2018). Even though clay is structurally not as strong as concrete, it might still be used for internal walls or claddings. This example shows that building scale additive manufacturing processes are not limited to concrete alone but can be transferred to other materials as well.

6.2. Future work

The main goal of this work was to show the feasibility of adding functionality to a 3D printed wall element using a simple design tool. Future work is necessary regarding the optimization of the developed cell structure. Both thermal and load bearing functions could potentially be further optimized by applying advanced simulation tools. Advanced simulation tools could be used to model the structural properties of the geometry both during the printing process and also in the hardened state under load.

The printing of the demonstrator objects showed that further research is necessary to predict the likelihood of collapsing overhangs. In the context of cell structures, the outermost cells of a printed element need specific attention as they seem to collapse more likely due to missing support from neighbouring cells. This also raises the question how the self-stabilizing behaviour of cell structures can be predicted.

When structural simulations are coupled with topology optimization algorithms, new potential regarding material savings could be exploited. Kontovourkis and Tryfonos already show a first implementation of topology optimization in a construction scale demonstrator printed from clay (Kontovourkis and Tryfonos, 2020).

Advanced thermodynamic flow simulation would be necessary to model the explicit convection related heat flux in the cell structure. Measurements could then verify the actual thermal performance of the building elements and recalibrate the simulation models specifically for 3D printed structures.

In order to prepare 3D printed cellular structures for the approval in building codes, future research is also necessary in regard to their moisture behaviour and fire protection.

7. Bibliography

3DPrint.com. (2016). *Chinese Construction Company 3D Prints an Entire Two-Story House On-Site in 45 Days*. [Online]. Available at: https://3dprint.com/138664/huashang-tengda-3d-print-house/ [Accessed 19 February 2020].

Agustí-Juan, I. and Habert, G. (2017). Environmental design guidelines for digital fabrication. *Journal of Cleaner Production*, 142, pp.2780–2791. [Online]. Available at: doi:10.1016/j.jclepro.2016.10.190 [Accessed 28 July 2019].

Ajdari, A. et al. (2012). Hierarchical honeycombs with tailorable properties. *International Journal of Solids and Structures*, 49 (11), pp.1413–1419. [Online]. Available at: doi:10.1016/j.ijsolstr.2012.02.029 [Accessed 14 August 2019].

Albrecht, W. and Schwitalla, C. (2015). *Rückbau, Recycling und Verwertung von WDVS: Möglichkeiten der Wiederverwertung von Bestandteilen des WDVS nach dessen Rückbau durch Zuführung in den Produktionskreislauf der Dämmstoffe bzw. Downcycling in die Produktion minderwertiger Güter bis hin zur energetischen Verwertung*, Forschungsinitiative ZukunftBau F 2932. Stuttgart: Fraunhofer-IRB-Verl.

Ankenbrand, H. (2015). Bauindustrie: Eine Villa aus dem 3D-Drucker. [Online]. Available at: https://www.faz.net/1.3466157 [Accessed 19 February 2020].

Apis Cor. (2019). *COLLABORATIVE PROJECT WITH DUBAI MUNICIPALITY*. [Online]. Available at: https://www.apis-cor.com [Accessed 19 February 2020].

Bankvall, C. G. (1972). NATURAL CONVECTIVE HEAT TRANSFER IN INSULATED STRUCTURES. *Division of Building Technology, Lund Institute of Technology*, p.9,55,100. [Accessed 16 March 2020].

Bekkouche, S. M. A. et al. (2013). *Thermal resistances of air in cavity walls and their effect upon the thermal insulation performance*. p.8.

Bos, F. et al. (2016). Additive manufacturing of concrete in construction: potentials and challenges of 3D concrete printing. *Virtual and Physical Prototyping*, 11 (3), pp.209–225. [Online]. Available at: doi:10.1080/17452759.2016.1209867 [Accessed 8 August 2019].

Buswell, R. A. et al. (2007). Freeform Construction: Mega-scale Rapid Manufacturing for construction. *Automation in Construction*, 16, pp.224–231. [Online]. Available at: doi:10.1016/j.autcon.2006.05.002.

Buswell, R. A. et al. (2018). 3D printing using concrete extrusion: A roadmap for research. *Cement and Concrete Research*, 112, pp.37–49. [Online]. Available at: doi:10.1016/j.cemconres.2018.05.006 [Accessed 28 July 2019].

Cesaretti, G. et al. (2014). Building components for an outpost on the Lunar soil by means of a novel 3D printing technology. *Acta Astronautica*, 93, pp.430–450. [Online]. Available at: doi:10.1016/j.actaastro.2013.07.034 [Accessed 23 January 2020].

Crump, S. S. (1992). *Apparatus and method for creating three-dimensional objects*. [Online]. Available at: https://patents.google.com/patent/US5121329/en [Accessed 12 February 2020].

De Schutter, G. et al. (2018). Vision of 3D printing with concrete — Technical, economic and environmental potentials. *Cement and Concrete Research*, 112, pp.25–36. [Online]. Available at: doi:10.1016/j.cemconres.2018.06.001.

Dennert Poraver GmbH. (2020). *Blähglas, der innovative Leichtzuschlag aus Recyclingglas.* [Online]. Available at: https://www.poraver.com/ [Accessed 2 March 2020].

DIN 4108-4. (2017). *Wärmeschutz und Energie-Einsparung in Gebäuden – Teil 4: Wärme- und feuchteschutztechnische Bemessungswerte*. Din Norm, DIN-Normenausschuss Bauwesen (NABau). [Accessed 21 February 2020].

DIN EN 206:2017-1. (2017). *DIN EN 206:2017-01, Beton_- Festlegung, Eigenschaften, Herstellung und Konformität; Deutsche Fassung EN_206:2013+A1:2016*. Beuth Verlag GmbH. [Online]. Available at: doi:10.31030/2584715 [Accessed 2 March 2020].

DIN EN ISO 6946. (2018). *Bauteile – Wärmedurchlasswiderstand und Wärmedurchgangskoeffizient – Berechnungsverfahren*. Din Norm, DIN-Normenausschuss Bauwesen (NABau). [Accessed 7 December 2019].

eurostat statistics. (2014). *File:Fatal and non-fatal accidents at work by economic activity, EU-28, 2014 (% of fatal and non-fatal accidents) YB16-II-de.png - Statistics Explained*. [Online]. Available at: https://ec.europa.eu/eurostat/statistics-

explained/index.php?title=File:Fatal_and_non-fatal_accidents_at_work_by_eco-nomic_activity,_EU-28,_2014_(%25_of_fatal_and_non-fatal_accidents)_YB16-II-de.png [Accessed 29 January 2020].

Gardiner, J. B. (2011). *Exploring the Emerging Design Territory of Construction 3D Print-ing.* [Online]. Available at: https://researchbank.rmit.edu.au/view/rmit:160277/Gardi-ner.pdf.

Goldman, R., Schaefer, S. and Ju, T. (2004). Turtle geometry in computer graphics and computer-aided design. *Computer-Aided Design*, 36 (14), pp.1471–1482. [Online]. Available at: doi:10.1016/j.cad.2003.10.005 [Accessed 25 February 2020].

Gosselin, C. et al. (2016). Large-scale 3D printing of ultra-high performance concrete – a new processing route for architects and builders. *Materials & Design*, 100, pp.102–109. [Online]. Available at: doi:10.1016/j.matdes.2016.03.097 [Accessed 8 August 2019].

Grashopper Primer V3.3. (2015). *Working With Attractors | The Grasshopper Primer Third Edition*. [Online]. Available at: https://modelab.gitbooks.io/grasshopper-primer/1-foundations/1-3/2_working-with-attractors.html [Accessed 25 February 2020].

Henke, K. et al. (2018). *Additive Fertigung von multifunktionalen, monolithischen Wan-delementen durch Extrusion von Leichtbeton (LC3D)*. Zwischenbericht, München: Tech-nische Universität München.

Henke, K., Talke, D. and Winter, S. (2016). *Additive Manufacturing of Building Elements by Extrusion of Wood Concrete*. In: 1 August 2016.

Henke, K., Talke, D. and Winter, S. (2017). *Multifunctional Concrete -Additive Manufac-turing by the Use of Lightweight Concrete*. In: 25 September 2017.

Hlaváč, V. (2019). *Robot trajectory generation*. Lecture, Czech Institute of Informatics, Robotics and Cybernetics.

Huizenga, C. et al. (1999). *THERM 2.0: a building component model for steady-state two-dimensional heat transfer*. In: 1999.

IPCC. (2014). *Climate Change 2014: Synthesis Report. Contribution of Working Groups I, II and III to the Fifth Assessment Report of the Intergovernmental Panel on Climate*

Change [Core Writing Team, R.K. Pachauri and L.A. Meyer (eds.)]. Geneva, Switzerland, p.151 pp. [Online]. Available at: https://www.ipcc.ch/report/ar5/syr/ [Accessed 2 March 2020].

Jin, Y. et al. (2014). Optimization of tool-path generation for material extrusion-based additive manufacturing technology. *Additive Manufacturing*, 1–4, pp.32–47. [Online]. Available at: doi:10.1016/j.addma.2014.08.004 [Accessed 30 August 2019].

Johnson, A. (2010). *Clipper - an open source freeware library for clipping and offsetting lines and polygons.* [Online]. Available at: https://github.com/eppz/Clipper [Accessed 16 March 2020].

Khoshnevis, B. (2004). Automated construction by contour crafting—related robotics and information technologies. *Automation in Construction*, 13 (1), pp.5–19. [Online]. Available at: doi:10.1016/j.autcon.2003.08.012 [Accessed 8 August 2019].

Khoshnevis, B. et al. (2006). *Mega-scale fabrication by Contour Crafting*. In: 2006. [Online]. Available at: doi:10.1504/IJISE.2006.009791.

Khoshnevis, B. and Bekey, G. (2002). *Automated Construction Using Contour Crafting -- Applications on Earth and Beyond*. In: 1 September 2002. Washington, DC, USA. [Online]. Available at: doi:10.22260/ISARC2002/0076 [Accessed 8 August 2019].

Khoshnevis, B. and Dutton, R. (1998). Innovative Rapid Prototyping Process Makes Large Sized, Smooth Surfaced Complex Shapes in a Wide Variety of Materials. *Materials Technology*, 13 (2), pp.53–56. [Online]. Available at: doi:10.1080/10667857.1998.11752766 [Accessed 6 February 2020].

Kontovourkis, O. and Tryfonos, G. (2018). *Integrating Parametric Design with Robotic Additive Manufacturing for 3D Clay Printing: An Experimental Study*. In: 22 July 2018. Taipei, Taiwan. [Online]. Available at: doi:10.22260/ISARC2018/0128 [Accessed 6 December 2019].

Kontovourkis, O. and Tryfonos, G. (2020). Robotic 3D clay printing of prefabricated non-conventional wall components based on a parametric-integrated design. *Automation in Construction*, 110, p.103005. [Online]. Available at: doi:10.1016/j.autcon.2019.103005 [Accessed 6 December 2019].

Kontovourkis, O., Tryfonos, G. and Georgiou, C. (2019). Robotic additive manufacturing (RAM) with clay using topology optimization principles for toolpath planning: the example of a building element. *Architectural Science Review*, pp.1–14. [Online]. Available at: doi:10.1080/00038628.2019.1620170 [Accessed 23 December 2019].

Kothman, I. and Faber, N. (2016). How 3D printing technology changes the rules of the game: Insights from the construction sector. *Journal of Manufacturing Technology Management*, 27 (7), pp.932–943. [Online]. Available at: doi:10.1108/JMTM-01-2016-0010 [Accessed 29 January 2020].

Lawrence Berkeley National Laboratory and National Fenestration Rating Council. (2015). *THERM 7 / WINDOW 7 NFRC Simulation Manual*. Lawrence Berkeley National Laboratory and National Fenestration Rating Council. [Online]. Available at: https://cdn.ymaws.com/nfrccommunity.site-ym.com/resource/resmgr/2014_Technical_Docs/NFRCSim7-May2015.pdf [Accessed 12 March 2020].

Le, T. T. et al. (2012). Mix design and fresh properties for high-performance printing concrete. *Materials and Structures*, 45 (8), pp.1221–1232. [Online]. Available at: doi:10.1617/s11527-012-9828-z [Accessed 31 January 2020].

Lehne, J. and Preston, F. (2018). *Making Concrete Change: Innovation in Low-carbon Cement and Concrete*. Chatham House. [Online]. Available at: https://reader.chathamhouse.org/making-concrete-change-innovation-low-carbon-cement-and-concrete [Accessed 24 January 2020].

Lim, S. et al. (2009). *FABRICATING CONSTRUCTION COMPONENTS USING LAYERED MANUFACTURING TECHNOLOGY*. p.11.

Lim, S. et al. (2011). *Development of a Viable Concrete Printing Process*. In: 2011. Seoul. [Online]. Available at: doi:10.22260/ISARC2011/0124.

Lim, S. et al. (2012). Developments in construction-scale additive manufacturing processes. *Automation in Construction*, 21, pp.262–268. [Online]. Available at: doi:10.1016/j.autcon.2011.06.010 [Accessed 8 August 2019].

Markforged, T. (2020). Metal X - revolutionären 3D-Drucker von Markforged jetzt online kaufen. *Mark3D Markforged 3D Drucker*. [Online]. Available at: https://www.mark3d.com/de/metalx/ [Accessed 6 February 2020].

Matthäus, C. et al. (2020). *Effect of Thixotropy Enhancing Agents on Extrudability of Lightweight Concrete*.

Mazur, M. et al. (2017). 5 - Mechanical properties of Ti6Al4V and AlSi12Mg lattice structures manufactured by Selective Laser Melting (SLM). In: Brandt, M. (Ed). *Laser Additive Manufacturing*. Woodhead Publishing Series in Electronic and Optical Materials. Woodhead Publishing. pp.119–161. [Online]. Available at: doi:10.1016/B978-0-08-100433-3.00005-1 [Accessed 6 February 2020].

McNeel & Associates. (2019). *Rhinoceros (Rhino) Version 6.0*. Barcelona: Robert McNeel & Associates. [Online]. Available at: https://www.rhino3d.com/de/ [Accessed 18 February 2020].

Nachtigall, W. and Wisser, A. (2013). *Bionik in Beispielen: 250 illustrierte Ansätze*. Berlin: Springer Spektrum.

Nammi, S. K. et al. (2014). *Verification of calculation code THERM in accordance with BS EN ISO 10077-2*. Research Report or Working Paper. [Online]. Available at: https://arro.anglia.ac.uk/332882/ [Accessed 12 December 2019].

Näther, M. et al. (2017). *Beton-3D-Druck - Machbarkeitsuntersuchungen zu kontinuierlichen und schalungsfreien Bauverfahren durch 3D-Formung von Frischbeton: Abschlussbericht*, Forschungsinitiative Zukunft Bau F 3024. Stuttgart: Fraunhofer IRB Verlag.

Ngo, T. D. et al. (2018). Additive manufacturing (3D printing): A review of materials, methods, applications and challenges. *Composites Part B: Engineering*, 143, pp.172–196. [Online]. Available at: doi:10.1016/j.compositesb.2018.02.012 [Accessed 29 January 2020].

Pandithevan, P. and Gurunathan, S. K. (2009). Personalised bone tissue engineering scaffold with controlled architecture using fractal tool paths in layered manufacturing. *Virtual and Physical Prototyping*, 4, pp.165–180. [Online]. Available at: doi:10.1080/17452750903055512.

Pegna, J. (1997). Exploratory investigation of solid freeform construction. *Automation in Construction*, 5 (5), pp.427–437. [Online]. Available at: doi:10.1016/S0926-5805(96)00166-5 [Accessed 11 February 2020].

Prasittisopin, L. et al. (2019). Lean Manufacturing and Thermal Enhancement of Single-Layered Wall of Additive Manufacturing (AM) Structure. *ZKG INTERNATIONAL*.

Réti, T. et al. (2020). *Modelling of Polycrystalline Microstructures Represented by Space-filling Polyhedral Cellular Systems*.

ryein and ecrlabs. (2019). *ecrlabs/dendro volumetric modelling for Rhino/Grasshopper*. Los Angeles, USA: ecr labs. [Online]. Available at: https://github.com/ecrlabs/dendro [Accessed 29 March 2020].

Sachs, E. M. et al. (1993). *Three-dimensional printing techniques*. [Online]. Available at: https://patents.google.com/patent/US5204055A/en [Accessed 12 February 2020].

Sadeghipour Roudsari, M. and Pak, M. (2013). *Ladybug: a parametric environmental plugin for grasshopper to help designers create an environmentally-conscious design.* In: 25 August 2013. Lyon, France. [Online]. Available at: http://www.ibpsa.org/proceedings/BS2013/p_2499.pdf [Accessed 13 March 2020].

South China Morning Post. (2017). *3D-printed or modular-built - China's construction revolutionaries*. [Online]. Available at: https://www.scmp.com/magazines/post-magazine/long-reads/article/2093914/we-could-3d-print-trumps-wall-china-construction [Accessed 19 February 2020].

Süddeutsche Zeitung. (2017). Ein Haus aus dem Drucker. [Online]. 31 August. Available at: https://www.sueddeutsche.de/geld/3d-ein-haus-aus-dem-drucker-1.3645991 [Accessed 18 February 2020].

UNEP. (2012). *Building Design and Construction: Forging Resource Efficiency and Sustainable Development*. UNEP Sustainable Buildings and Climate Initiative. [Online]. Available at: https://s3.amazonaws.com/legacy.usgbc.org/usgbc/docs/Archive/General/Docs19073.pdf [Accessed 2 March 2020].

Wangler, T. et al. (2016). Digital Concrete: Opportunities and Challenges. *RILEM Technical Letters*, 1, p.67. [Online]. Available at: doi:10.21809/rilemtechlett.2016.16 [Accessed 28 July 2019].

Weisstein, E. W. (2017). *Truncated Octahedron*. [Online]. Available at: http://mathworld.wolfram.com/TruncatedOctahedron.html [Accessed 11 February 2020].

Wells, D. G. (1991). *The Penguin dictionary of curious and interesting geometry*. London, England ; New York, N.Y., USA: Penguin Books.

WinSun3D. (2013). *News-Yingchuang Building Technology (Shanghai) Co., Ltd.* [Online]. Available at: http://www.winsun3d.com/News/news_inner/id/515 [Accessed 19 February 2020].

WinSun3D. (2019). *Winsun 3D R&D Center in Shanghai - Largest 3D Printing Building Construction*. [Online]. Available at: https://www.youtube.com/watch?v=phL3RNsRpTw [Accessed 18 February 2020].

WinSun3D. (2020). *Product Center-Yingchuang Building Technique （Shanghai）Co.Ltd. (WinSun)*. [Online]. Available at: http://www.winsun3d.com/En/Product/pro-list/id/1 [Accessed 18 February 2020].

Woensel, R. N. P. van et al. (2018). Printing Architecture: an overview of existing and promising additive manufacturing methods and their application in the building industry. *The International Journal of the Constructed Environment*, 9 (1), pp.57–81. [Online]. Available at: doi:10.18848/2154-8587/CGP/v09i01/57-81 [Accessed 19 August 2019].

XtreeE. (2016). *Post in Aix-en-Provence | XtreeE*. [Online]. Available at: http://www.xtreee.eu/post-in-aix-en-provence/ [Accessed 20 February 2020].

8. List of figures

9. List of tables

Appendix A   Design Tool

The design tool developed within this thesis was developed within the Python programming language and graphical scripting environment of Grasshopper (McNeel & Associates, 2019). The grasshopper tool as well as the python code used to calculate the print paths for cellular structures are provided as a Github repository. The package is called 'cellmaker' and is provided under the following link: https://github.com/augmentedfabricationlab/cellmaker

Install the following dependencies to run the design tool:

- Rhinoceros 6.0 and Grasshopper (McNeel & Associates, 2019)

- The 'cellmaker' package: Add path python files to the Grasshopper Python library folder by typing 'Grasshopper Developer Settings' in the Rhino command line or add the package to the python path variable

- Dendro volumentric modeling plugin for preview renderings of geometries

- Clipper, LBNL Therm 7.6 and Honeybee&Ladybug for thermal simulations

Figure 37 below shows on overview of the design tool in the Grasshopper environment. The main feedback indicator values are given as component messages directly on the canvas. Layer cycle times and overhangs can additionally be visualized as false-color renderings.
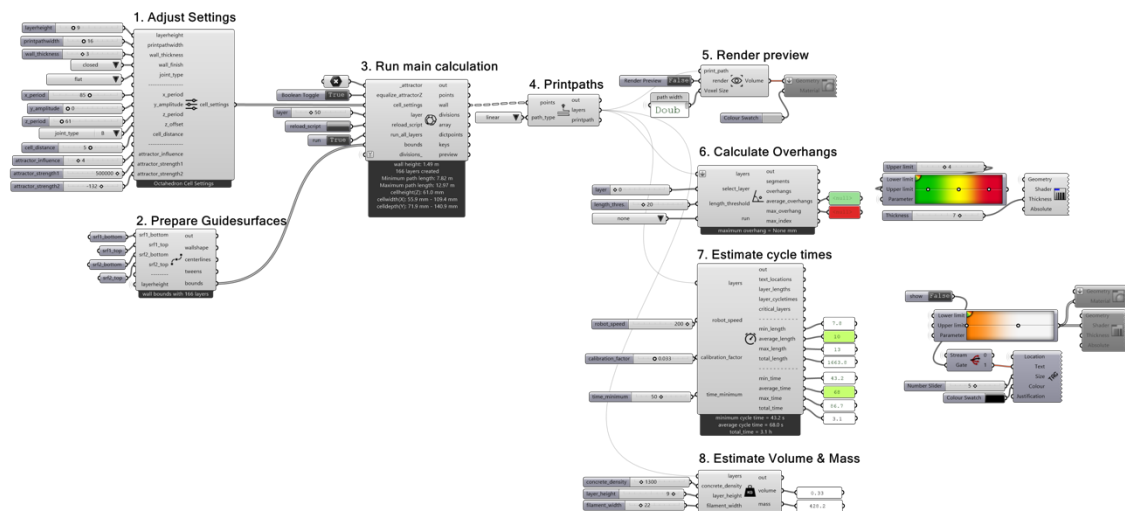
Figure 37: Design tool structure in Grasshopper environment

The grasshopper tool is structured in the following components:

Component icon	Component name	Function
	Cell settings	Adjust cell and print settings like layer height, filament width, cell size, cell density, joint type, correction factors, wall finish and attractor settings
	Prepare guide surfaces	Calculate boundary curves for the print path modeling based on two input guide surfaces
	Define attractor point	Define and adjust an attractor point to adjust the cell sizes gradually along the guide surfaces
	Run main calculation	Run the main print modelling. The core python library is imported inside this component
	Interpolate print paths	Interpolate print paths from control points
	Render preview	Render a preview of a design using the Dendro volumetric modelling plugin (ryein and ecrlabs, 2019)
	Calculate overhangs	Calculate overhangs, visualize them in the model and get maximum overhang per layer
	Estimate cycle times	Estimate the cycle times per layer and total printing time based on path length and curvature

	Estimate volume & mass	Estimate the concrete volume and mass based on path length and filament geometry
	Create section view	Create a section through a wall element. Can be useful to understand the cell geometry or perform further simulations
	THERM simulation	Estimate the heat transfer coefficient of a specific location in a wall element. This is a cluster containing the simulation based on Honeybee components and the clipper library. (Sadeghipour Roudsari and Pak, 2013; Johnson, 2010; Lawrence Berkeley National Laboratory and National Fenestration Rating Council, 2015)

Appendix B   Python code documentation

When you do want to import the Python-code used in the Grasshopper tool into your own components follow the following steps:

Before starting, install the Python package 'cellmaker' and its dependencies as described in Appendix A.

Then, import the basic Rhino.Geometry library and the main LayerFromGuide class:

```python
import Rhino.Geometry as rg
from cellmaker.octahedron import LayerFromGuide
```

And set some properties of the layers as class variables:

```python
# set some properties for the print paths
LayerFromGuide.bounds = boundary_curves
LayerFromGuide.outsideclose = True
LayerFromGuide.thickness = 5  # millimeters
LayerFromGuide.pwidth = 22  # millimeters
LayerFromGuide.zperiod = 180  # millimeters
```

These class variables will used for all the layer instances created afterwards. Most of the variables have preset values to allow an easy start with the tool. You can simply override these presets by setting new values for the class variables. In Grasshopper and Visual Studio Code, all the class variables can be accessed with the dot operator:


```
LayerFromGuide.|
                 OctahedronVectorsForS
                 outsideclose
                 pwidth
                 redefine_xperiod
                 strength1
                 strength2
                 thickness
                 xperiod
                 yamplitude
                 zperiod
```
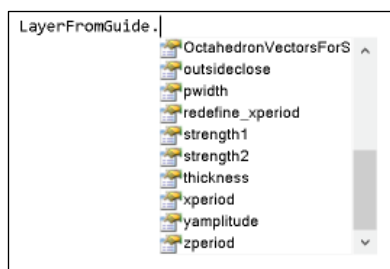
Figure 38: Dot operator revealing the LayerFromGuide class variables

You can then calculate a first print path layer by invoking a first print path layer instance:

```python
# invoke a first print path layer instance
z_height = 9
LayerFromGuide(z_height)
```

To calculate the print paths of an entire wall element, make a list of boundary curves first. Provide the curves as pairs for each layer in a list of lists. You can do this by using the CreateWallshape function:

```python
centerlines,bounds,tweens = create_layerbounds_from_wallshape(wallshape,layerheight)
```
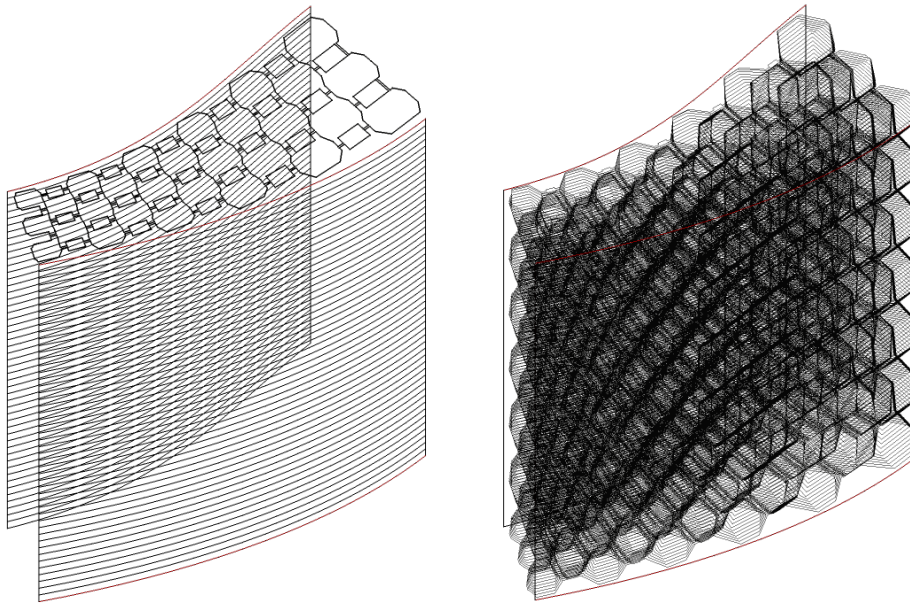
Figure 39: Guidesurfaces split into boundary curves (left) and print paths calculated for an entire wall element (right)

Then, calculate the layers from the list of boundary curves and append the control points to a list.

```
# calculate the print paths of an entire wall element
wall = []
for bounds in boundslist:
    LayerFromGuide.bounds = bounds
    z_height = bound[1].PointAtStart.Z
    layer = LayerFromGuide(z_height)

    wall.append(layer.singlelayer)
```

To perform a feedback calculation on the calculated print paths, import whatever feedback you need from cellmaker.feedback:

```
# calculate overhangs
from cellmaker.feedback import GetOverhangs

overhangs, max_overhang, segments, max_index, average_overhangs = GetOverhangs(layers, length_threshold)
```

Converting nested lists to trees using 'ghpythonlib.itertools' may be required to see the geometry in Grasshopper.

For a detailed description of class options and methods, all the methods contained in the cellmaker package are documented below:

cellmaker.feedback module

Collection of useful functions to analyze print paths of cellular structures

cellmaker.feedback.GetOverhangs(*layers, length_threshold*)

Calculates overhangs from layer to layer for a wall assembly.

Parameters:	**layers** – list of polylines or curves
Returns:	Overhangs for every print path polyline segment Maximum overhang of all the layers Segements for visulaisation purposes

cellmaker.feedback.estimate_cycletime(*layer, robot_speed, calibration_factor*)

Estimate the expected layer cycle time in the printing process. As the robot decelerates and accelerates in corners, layer cycle times are estimated based on path length and total degree and number of directional changes in the print path.

Parameters:	**printpaths** – list of printpaths of layers **robot_speed** – speed of the robot in mm/s **calibration_factor** – a factor specific for a certain robot model. Calculate this by comparing predicted with measured cycle times
Returns:	Estimated Layer Cycle times

cellmaker.feedback.get_mass_from_geo(*layers, concrete_density, layer_height, filament_width*)

Estimate volume and mass based on printpath and filament geometry.

Parameters:	**layers** – print paths provided as list of layers **concrete_density** – kg/m3, e.g: 1.300 kg/m3 for lightweight concrete **layer_height** – mm, e.g. 9mm **filament_width** – mm, e.g. 22mm
Returns:	concrete volume in m3 concrete mass in kg

cellmaker.octahedron module

The core print path modelling module containing all the functions to calculate print paths based on the shape of a truncated octahedron.

Class cellmaker.octahedron.LayerFromGuide(*zheight, divisions=None*)

> Creates a single layer from an octahedron cell array in between two boundary curves. Every instance is initiated with some preset values to get an output with a minimum of inputs.

> **Presets:**

> attractor = rg.Point3d(5, 1, 0) strength1 = 10000 strength2 = 100 influence = 5 bounds = [] lheight = 9 pwidth = 22 outsideclose = True celldist = 5 # CELL SHAPE yamplitude = 0 xperiod = 50 zperiod = 300 thickness = 6 divcountsIN = None # [15,[5,5]] mincellwidth = 2 * pwidth start_half = 1

> **Parameters:**
> - **zheight** (*float*) – The current position in z direction (height), mandatory input!
> - **divisions** – Provide cell divisions in x direction as manual input, replaces attrator calculation
> - **attractor** – Point to adjust the gradient of cell sizes along a guidecurve
> - **strength1** – Strength of the attractor, a value of 10000 is preset
> - **strength2** – Strength of the attractor, a value of 10000 is preset
> - **influence** – Number of cells that are influenced by the attrator.
> - **divcountsIN** – Provide attractor settings as manual input in the form of: [15,[5,5]] Where the first number is the pointindex closest to the attractor and the following numbers the influence of the attractor
> - **bounds** – List of boundary curves derived horizontal section of guidesurfaces
> - **lheight** – the height of the layers, usually the desired filament thickness, preset to 9mm

- **pwidth** – width of the print path or nozzle, preset to 22mm
- **outsideclose** – Boolean value to determine wether outside cells are open or closed
- **celldist** – Correction factor to compensate discrepancy between model and physical reality caused by robot dynamics
- **# CELL SHAPE**
- **yamplitude** – Size of the cells in y direction (perpendicular to guidecuvre)
- **xperiod** – Size of the cells in x direction (parallel to guidecuvre)
- **zperiod** – Height of the cells (period of zigzag function)
- **thickness** – Number of cells in x direction, meaning the density of cells
- **mincellwidth** – The minimal width of the cells, usually this is 2 * pwidth
- **start_half** – start the vector sequence with half in y direction. Set this to True if you want to have nice joints

CellsAlongCurve(*row, yvals, yamplitudes, direction, loop, xpoints, normal*)

Create cells of Octahedron shape in thickness layers along guidecurve segments.

Parameters:
- **yvals** (*list*) – list of lists from Octahedron Vectors
- **yamplitudes** (*list*) – list from Curvestartoffsetttractor
- **direction** (*bool*) – Boolean, 1 = forward travel in thickness layer
- **loop** (*int*) – iterator position of thickness layer
- **xpoints** (*array*) – list of lists of division points for subcurves
- **normals** (*array*) – list of lists of normals for points on subcurves

Returns:
pointsarray, pointsdict – Array of control points for print path generation and points dictionary with cell names

CreateOctahedronJoint(*lastsubcurve, lastyamplitude, side=0*)

Creates jointsequence of vectors to form octahedron shape like element joints.

Parameters:	• **lastsubcurve** (*curve*) – subcurve to which the joint shall be added to
	• **lastyamplitude** (*float*) – y amplitude of joint
	• **side** – 0 = Start, 1 = End

Returns:	Jointsequence of vectors which can be used to model a joint in octahedron logic

CreateOctahedronVectors(*subcurve, size, yamplitude, outsideclose=False*)

Creates a vector sequence in Octahedron Shape.

Parameters:	• **guide** (*curve*) – defining the period of the cell in x direction
	• **size** (*float*) – size or equivalent z value for cell size
	• **outsideclose** (*bool*) – return vector pattern for outside layer of wall

Returns:	*vectorsequence (list)* – vectors of octahedron printpath

CreateWallshapeGuidecurves(*wallshape, layerheight*)

Calculate layer boundary curves from a wallshape provided as guidesurfaces

Parameters:	• **wallshape** – wallshape defined by two boundary surfaces
	• **layerheight** – desired height of the layers in mm

Returns:	*centerlines* – the centerline between the boundary curves in every layer bounds: a list of lists of bounds where the boundary curves are provided pairwise per layer tweens: a flattened list of the bounds list of lists

CreateZVals(*srf*)

Creates Z-Values from Guidesurface and layer height

OctahedronVectorsForSubcurves(*subcurves, yamplitudes, outsideclose=False*)

Iterates over subcurves and returns X and Y values of Octahedron vector sequence.

Parameters:	• **subcurves** – list of subcurves from main guidecurve for layer
	• **yamplitudes** – list of yamplitudes for subcurves
	• **outsideclose** – bool to make cells on outermost layer closed.

create_guide_from_bounds**( )**

This function creates a centerline between two boundary curves and shortens it to leave space for element joints.

create_octahedron_layer**( )**

This function just unites all necessary steps to create Octahedron printpath layers.

1. Divide guidecurve into subcurves which represent the cell divisions in x direction.
2. Calculate y amplitudes of cells as distance from centerline to boudaries.
3. Store vector sequence of octahedron print paths
4. Calculate forward and backward print path loops to make continous print path.
5. Add Element joints

redefine_xperiod**(*subcurve*)**

Redefines the xperiod for octahedron vectors based on the subcurve length.

| Parameters: | **subcurve** (*curve*) – A subcurve from main guidecurve. |

| Returns: | period of the cells in x direction. This is usuallay the direction along the guidecurve |

cellmaker.useful module

Collection of useful functions to perform geometrical operations for print path modelling.

cellmaker.useful.ConvertParamToLength(*curve, parameter*)

Converts a curve parameter to a Length parameter

cellmaker.useful.CurveClosestPoint(*guide, point*)

Snaps a point to the closest point on a curve or polyline

Parameters:
- **guide** – curve or polyline
- **point** – reference point to search from

cellmaker.useful.CurveDivideEqual(*guide, divisionlength*)

This function divides a curve by a given length without leaving a remainder. If the remainder is greater than half the division length, an additional division is added.

cellmaker.useful.CurveMidpoint(*curve*)

Calculate the midpoint of a curve segment.

cellmaker.useful.CurveOffsetByAttractor(*guidecurve, attractor, divisionpoints, offset*)

Offset a curve relative to an attractor point. The input curves control points are offset antirelative to the distance to an attractor point.

Parameters:
- **guidecurve** – guidecurve to perform offset on
- **attractor** – attrator point
- **divisionpoints** – initial division points on curve
- **offset** – distance to offset

Returns:
- Offset and reshaped curve
- Offset distances of control points

cellmaker.useful.CurvePointGetLength(*curve, point*)

Returns the length parameter of a point on a curve.

cellmaker.useful.CurvePointMoveLength(*curve, point, lengthtomove*)

Move a point along a curve by a given length.

cellmaker.useful.CurvePointOffset(*guide, xparts, yparts*)

This function creates division points along a curve based on a list of length parameters. A list of y values is then used to offset those points perpendicular to the guidecurve.

Parameters:	• **guide** – curve • **xparts** – list of curve length parameters from GetVectorX function • **yparts** – list of curve length parameters from GetVectorY function

cellmaker.useful.CurvePointsStretch(*curve, points*)

Stretch points on a curve to eliminate the remainder at the end. Takes a list of points, calculates the remainder in the end and moves every point to close the gap.

cellmaker.useful.DivideCurveAttractor(*guide, attractor, xperiod, strength1, strength2, influence, divcountsIN=None*)

This method adds division points with a gradient controlled by an attractor.

Parameters:	• **guide** (*curve*) – the guidecurve object • **attractor** (*point*) – a point • **attrsettings** (*list*) – a list of divisionlength, strength1, strenght2, influence • **divcountsEXT** (*list*) – optional input if certain pointcount is desired
Returns:	*pointsnew(list)* – the actual divisionpoints lines(list): lines from initial points to attractor pulledpoints(list): pulled points points(list): initial division points

cellmaker.useful.FlattenList(*list_of_lists*)

Flatten a list of lists using python itertools.

cellmaker.useful.GetRelative(*vector, curve, point_or_parameter*)

Orients a vector relative to the tangent vector of a guidecurve. A point or a curve parameter can be given as a reference. The reference point is the closest point from the given point on the guidecurve.

Parameters:	• **vector** – The vector to orient
	• **curve** – the reference curve
	• **point_or_parameter** – point or parameter in reference curve

cellmaker.useful.GetVectorX(*hvectors*)

This function returns the X values of a vector sequence as partial results of a mass addition.

cellmaker.useful.GetVectorY(*hvectors*)

This function returns the Y values of a vector sequence as partial results of a mass addition.

cellmaker.useful.LineMidpoint(*line*)

Calculate the midpoint of a line

cellmaker.useful.ListRemoveValue(*valuelist, value_to_remove*)

Remove all occurences of a value from a list

cellmaker.useful.MassAddition(*values, return_partial_results=True*)

Perform massaddition of xvals and return partial results

cellmaker.useful.NegateListOfLists(*listoflists*)

Negate all the values in a list of lists.

cellmaker.useful.NormalAt(*curve, point_or_parameter*)

Returns the normal of a curve at a parameter or point on curve

cellmaker.useful.OrientVectorX(*vector, target*)

This function orients a vector based on a target plane X axis. World X axis is regarded as reference

Parameters:	• **vector**
	• **targetx** (*vector*) – target vector describing the x axis of the target coordinate system.

cellmaker.useful.OrientVectorY(*vector, target*)

This function orients a vector based on a target plane Y axis. World Y axis is regarded as reference.

Parameters:	• **vector**
	• **targetx** (*vector*) – target vector describing the y axis of the target coordinate system.

cellmaker.useful.PointCloudClosestPoint(*points, testpoint*)

Retrieve the closest point to a testpoint from a pointlist

cellmaker.useful.PointsAttractorDistances(*attractor, divisionpoints*)

Calculate distances between a pointlist and a point.

cellmaker.useful.PointsOffsetDirection(*points, directions*)

This function moves a list of points along a list of vectors.

Parameters:	• **xparts** – list of curve length parameters from GetVectorX function
	• **yparts** – list of curve length parameters from GetVectorY function

cellmaker.useful.PrintPoints(*points*)

Print points to the "out" output of a grasshopper component

cellmaker.useful.SortListBasedonList(*referencelist, list_to_besorted*)

Sort a list of values or objects based on a sortable list of reference values.

cellmaker.useful.SubcurveDivisionsWithNormals(*subcurves, xvals*)

Operates on a list of x val lists and returns divisionspoints and normals for subcurves.

Parameters:	• **subcurves** – list of subcurves
	• **xvals** – list of lists with division distanes from Octahedron Vectors

cellmaker.useful.ZigZagVal(*period, x, phaseshift=0, dx=0*)

Zigzag is a zigzag function. It can be described as a linearized sine function.

Parameters:	• **period** (*float*) – the period of the periodic function
	• **x** (*float*) – the x value to compute
	• **phaseshift** (*bool*) – True if function is supposed to be shiftet in x direction
	• **dx** (*bool*) – True if you want to calculate the 1st derivative of the function

Returns:	Function value of a linearized zig zag function

cellmaker.useful.projected_distance(*point1, point2*)

Calculates the distance between two points projected in the XY-Plane